Chapter 4

EFFECTS OF AMINOPHOSPHINE LIGANDS ON RUTHENIUM OLEFIN METATHESIS CATALYST ACTIVITY

This work was performed in collaboration with Dr. Tzu-Pin Lin, who contributed to project design, catalyst synthesis and characterization, and kinetics experiments, and Dr. Allegra Liberman-Martin, who performed ROMP studies. All related computational studies were performed by Huiling Shao and Professor Peng Liu from the University of Pittsburgh.

Abstract

Second-generation ruthenium olefin metathesis catalysts bearing aminophosphine ligands were investigated with systematic variation of the ligand structure. The rates of phosphine dissociation (k_1; initiation rate) and relative phosphine reassociation (k_{-1}) were determined for two series of catalysts bearing cyclohexyl(morpholino)phosphine and cyclohexyl(piperidino)phosphine ligands. In both cases, incorporating P–N bonds into the architecture of the dissociating phosphine accelerates catalyst initiation relative to the parent complex (–PCy_3); however, this effect is muted for the tris(amino)phosphine-ligated complexes, which exhibit higher ligand binding constants in comparison to those with phosphines containing one or two Cy substituents. These results, along with X-ray crystallographic data and DFT calculations, were used to understand the influence of ligand structure on catalyst activity. Especially noteworthy is the application of phosphines containing incongruent substituents ($PR_1R'_2$); detailed analyses of factors affecting ligand dissociation, including steric effects, inductive effects, and ligand conformation, are presented. Computational studies of the reaction coordinate for ligand dissociation reveal that ligand conformational changes in the transition state contribute to rapid dissociation for the fastest initiating catalyst of these series, which bears a cyclohexyl-bis(morpholino)phosphine ligand. Furthermore, the effect of amine incorporation was also examined in the context of ring-opening metathesis polymerization, and reaction rates were found to correlate well with catalyst initiation rates. The combined experimental and

computational studies presented reveal important considerations for promoting phosphine dissociation in ruthenium olefin metathesis catalysts.

Introduction

Since its discovery in the 1950s, olefin metathesis has evolved into a versatile and powerful reaction for organic synthesis.[1] Molybdenum, tungsten, and ruthenium catalysts have been extensively investigated in the synthesis of natural and unnatural products, including the formation of substituted olefins and cyclic organic compounds.[2] Furthermore, significant efforts toward the development of olefin metathesis polymerizations,[3] notably ring-opening metathesis polymerization (ROMP)[4] and acyclic diene metathesis (ADMET),[5] have enabled the synthesis of new functional materials[6] and have led to important industrial applications.[7]

Complexes based on molybdenum and tungsten were the earliest reported well-defined olefin metathesis catalysts, and since their initial discovery, have been widely used for their high reactivity.[8] Extensive research of ruthenium-based complexes has resulted in metathesis catalysts with increased functional group tolerance and stability to air and moisture. Demonstration of ruthenium alkylidene complexes as viable olefin metathesis catalysts[9] led to the development of catalyst **4-1** (Figure 4.1).[10] The lower activity of **4-1** in comparison to molybdenum catalysts was later addressed by our group through the development of second-generation ruthenium olefin metathesis catalysts, notably **4-2**,[11] in which a phosphine is substituted for an *N*-heterocyclic carbene (NHC) ligand.[12,13] The bispyridine complex **4-3** and related complexes have proven to be fast-initiating, enabling cross metathesis of challenging substrates[14] and ROMP to produce polymers with controllable molecular weight and low dispersity;[15] additionally, complex **4-3** can serve as a useful precursor for variants of catalyst **4-2** that bear a variety of organic substituents on the dissociating phosphine.[16]

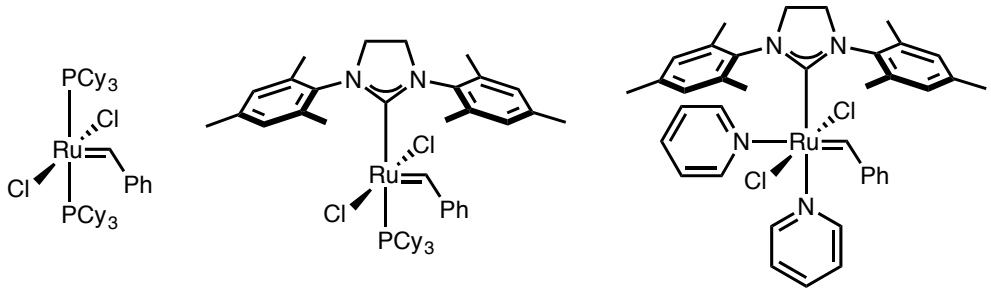

4-1 **4-2** **4-3**

Figure 4.1. Established Ruthenium Olefin Metathesis Catalysts.

Mechanistic studies of olefin metathesis promoted by second-generation ruthenium catalysts have suggested that these reactions occur by a dissociative pathway, in which phosphine dissociation occurs to form a 14-electron intermediate in an initiation step prior to olefin binding (Scheme 4.1).[17] Thus, the activity of these catalysts is affected by the rate of phosphine dissociation (k_1; initiation rate) and the relative rate of phosphine reassociation (k_{-1}). Following formation of the 14-electron intermediate, the likelihood of phosphine reassociation versus productive olefin binding (k_{-1}/k_2) can be experimentally determined; higher selectivity for binding of the olefin over the phosphine, rather than higher initation kinetics, has been shown to be the underlying cause for increased activity of **4-2** compared to **4-1**.[18]

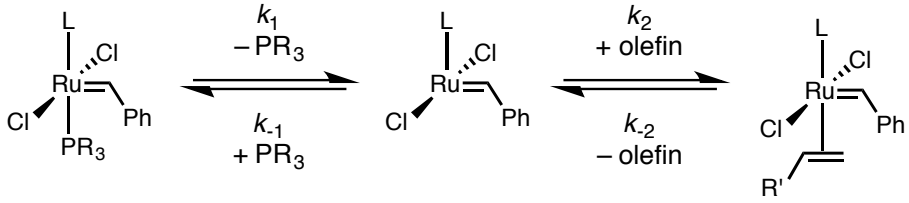

Scheme 4.1. Proposed Dissociative Mechanism for Second-Generation Ruthenium Olefin Metathesis Catalysts.

Rate constants have been reported for a variety of second-generation ruthenium catalysts bearing phosphine ligands with different substituents.[19] While phosphine electronics have been shown previously not to directly correlate with phosphine reassociation, initiation rates are known to increase with decreasing σ-donating ability of the phosphine. With this in mind, we became interested in further exploring phosphines

that are weak σ-donors as ligands for second-generation catalysts. While phosphines containing halogenated arenes have been investigated, the incorporation of P–X bonds, where X is an electron-withdrawing heteroatom, has been much less explored in this context. Such ligands have been broadly applied in organometallic chemistry, spanning a wide range of accessible σ-donating and π-accepting properties.[20] NMR studies of aminophosphines, with structure $P(NR)_3$, have demonstrated decreased σ-basicity of these ligands in comparison to triphenylphosphine.[21] Due to the electronic properties and ease of preparation of aminophosphines, these ligands are particularly well suited to systematically investigate the incorporation of P–X bonds to increase catalyst activity. The kinetics and computational studies described herein demonstrate the importance of several key factors in promoting phosphine dissociation, facilitating the design of new ligands for efficient ruthenium olefin metathesis catalysts.

In this study, nitrogen-containing heterocycles were systematically introduced in place of the cyclohexyl groups in complex **2** to probe the effect of P–N bonds on catalyst activity. NMR spectroscopic and X-ray crystallographic data were obtained to gather structural information, and these data were analyzed in the context of kinetics studies. Initiation rates and the relative phosphine reassociation rates were measured, together providing a metric to compare aminophosphine binding strengths. Trends in ligand binding strengths and initiation rates agree well with DFT calculations, which account for important parameters affecting ligand properties. Furthermore, the use of phosphines bearing incongruent substituents allows for a more comprehensive understanding of ligand structure, providing additional information regarding the effects of sterics and ligand conformation on phosphine dissociation. Simple substitution of nitrogen and oxygen atoms in the ligand composition of complex **2** delivered over an order of magnitude increase in catalyst initiation rates, which directly correlate with rates of conversion in ROMP studies.

Ligand and Catalyst Synthesis and Characterization

Two new series of second-generation ruthenium olefin metathesis catalysts bearing aminophosphine ligands in place of the tricyclohexylphosphine present in catalyst **4-2** were synthesized. Morpholine and piperidine substituents were incorporated to decrease

phosphine donor strength through the introduction of P–N bonds due to their similar size to cyclohexane, and complexation of these aminophosphines led to the formation of six new catalysts **4-4** through **4-9** (Figure 4.2).

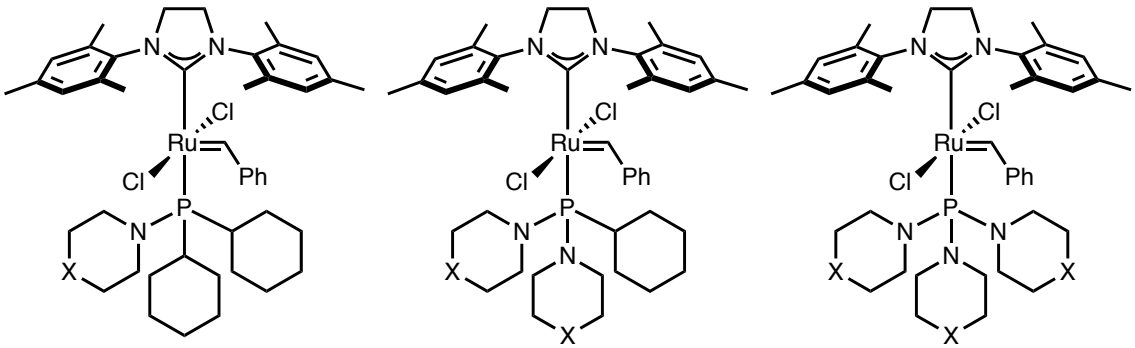

4-4 (X = O)
4-7 (X = CH_2)

4-5 (X = O)
4-8 (X = CH_2)

4-6 (X = O)
4-9 (X = CH_2)

Figure 4.2. New Ruthenium-Based Olefin Metathesis Catalysts Bearing Aminophosphine Ligands Derived from Morpholine and Piperidine.

Treatment of the appropriate chlorocyclohexylphosphine or trichlorophosphine starting materials with excess morpholine or piperidine produced the corresponding aminophosphines **4-10** through **4-15** (Scheme 4.2A). Following successful synthesis of the desired ligands, complexation to form catalysts **4-4** through **4-9** was achieved by reacting the bis(pyridine) catalyst **3** with an excess of aminophosphine in THF (Scheme 4.2B), modified from a previously reported procedure.[16]

Second-generation ruthenium olefin metathesis catalysts with aromatic phosphine ligands are known to be faster initiating than their alkylphosphine counterparts, and the effects of replacing the PCy_3 ligand with PPh_3 in **4-2** and related catalysts have been well-studied for ring-closing metathesis (RCM)[22] and ROMP[19a] reactions. Thus, following the successful synthesis of catalysts **4-4** through **4-9**, we became interested in potentially faster initiating species derived from aromatic amines. A pyrrolylphosphine ligand **4-16** was synthesized by a procedure modified from that shown in Scheme 4.2. Synthesis and characterization for **4-17** can be found in the Experimental Section.

A) Synthesis of Aminophosphine Ligands

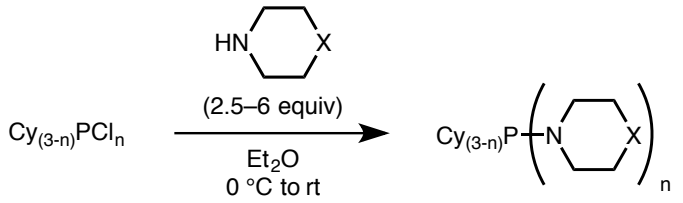

4-10 (n = 1; X = O) **4-13** (n = 1; X = CH_2)
4-11 (n = 2; X = O) **4-14** (n = 2; X = CH_2)
4-12 (n = 3; X = O) **4-15** (n = 3; X = CH_2)

B) Representative Complexation to Generate Catalyst 4-4

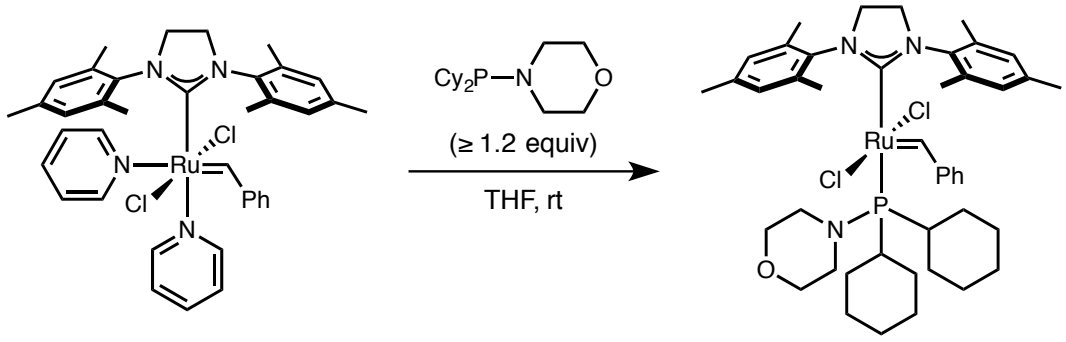

4-3 **4-4**

Scheme 4.2. Synthetic Route to Prepare Complexes **4-4** Through **4-9**.

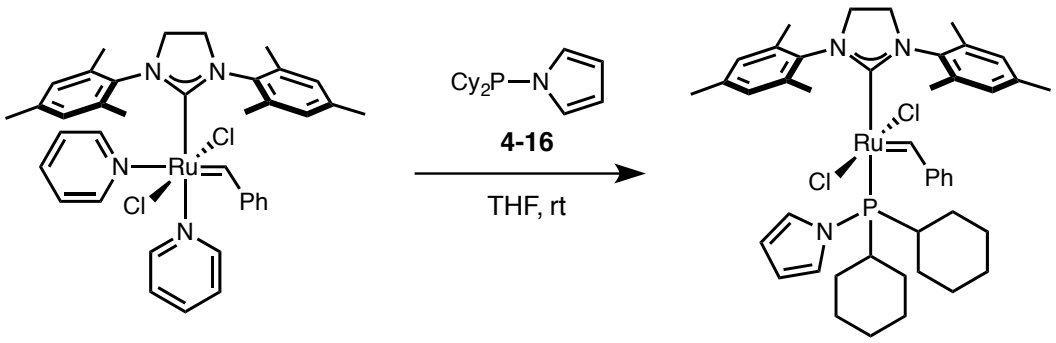

4-3 **4-17**

Scheme 4.3. Synthesis of a Ruthenium-Based Olefin Metathesis Catalyst Bearing a Pyrrolylphosphine Ligand.

All catalysts described in this report were characterized by ^{1}H, ^{13}C, and ^{31}P NMR as well as high-resolution mass spectrometry. Furthermore, X-ray crystallography was performed for certain complexes to compare selected bond lengths and angles within a

series of new catalysts. Trends observed in the characterization of these compounds are discussed below, with further data described in the Experimental Section.

The ^{31}P NMR shifts for catalysts **4-2**, **4-4** through **4-9**, and **4-17** were compared along with those for the corresponding free phosphine ligands (Table 4.1). In both the morpholine- and piperidine-based series, the chemical shift for the free phosphine becomes more downfield as amine substitution increases. However, following complexation, this trend is not observed in the case of ^{31}P NMR shifts for the ruthenium catalysts. While the phosphorus nuclei are significantly deshielded in the mono- and bis(amino)phosphine cases (Δppm > 16 ppm), the phosphorus nuclei of the tris(amino)phosphine-ligated catalysts are far less deshielded following complexation (Δppm ~ 2 ppm).

Table 4.1. Signature ^{31}P NMR Shifts of Free Aminophosphines and Catalysts[a]

catalyst	cat. (^{31}P)	ligand	free ligand (^{31}P)	Δ ppm
4-2	29.4	PCy_3	8.8	20.6
4-4	92.4	**4-10**	75.6	16.8
4-5	131.9	**4-11**	98	33.9
4-6	116.7	**4-12**	114.7	2.0
4-7	92.1	**4-13**	75.9	16.2
4-8	133.0	**4-14**	98.8	34.0
4-9	118.7	**4-15**	116.8	1.9
4-17	92.3	**4-16**	66.1	26.2

[a]All samples prepared in C_6D_6.

Catalysts **4-7** through **4-9**, containing piperidine-substituted phosphine ligands, as well as catalyst **4-17** were selected for further characterization by X-ray crystallography. The structures of **4-7** through **4-9** and **4-17** are shown in Figures 4.3-4.6. The crystal structures confirm the connectivity expected for the phosphine-ligated complexes. Selected bond lengths and bond angles of catalysts **4-2** and **4-7** through **4-9** are displayed in Table 4.2 for comparison within a single series.

In each case, the catalysts in Figures 4.3-4.6 crystallize in such a way that one substituent on the phosphine ligand occupies a pseudo-equatorial position and is oriented

away from the benzylidene. Complexes **4-8** and **4-9** are distinguished in that a piperidine ring occupies this position (Figures 4.4 and 4.5), whereas in cases in which only one amine group is present, one of the two cyclohexyl rings will take this position (Figures 4.3 and 4.6). All catalysts within the piperidine series (**4-7** through **4-9**) have similar Ru–C1 bond lengths when compared to that of the parent catalyst **4-2** (Table 4.2). The length of the Ru–C8 bond increases as piperidine substitution is systematically introduced. Additionally, the Ru–P bond of catalyst **4-7**, with one piperidine substituent, is longer than that of catalyst **4-8**, which contains two piperidine rings; these Ru–P bond lengths show no direct correlation with the rate of phosphine dissociation (*vide infra*).

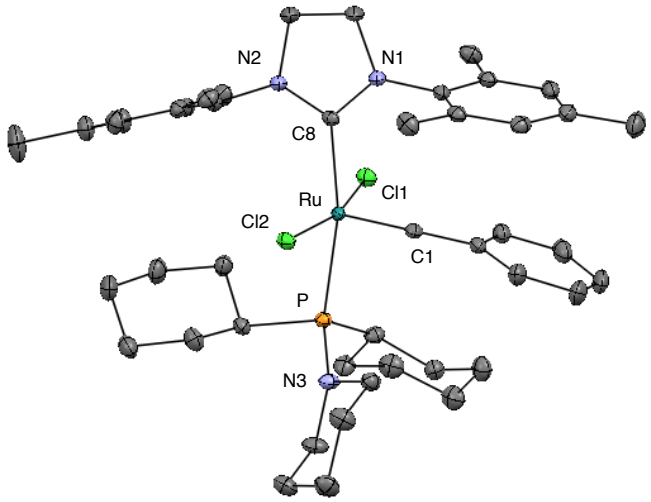

Figure 4.3. X-ray crystal structure of catalyst **4-7** with 50% probability ellipsoids. Hydrogen atoms have been omitted for clarity.

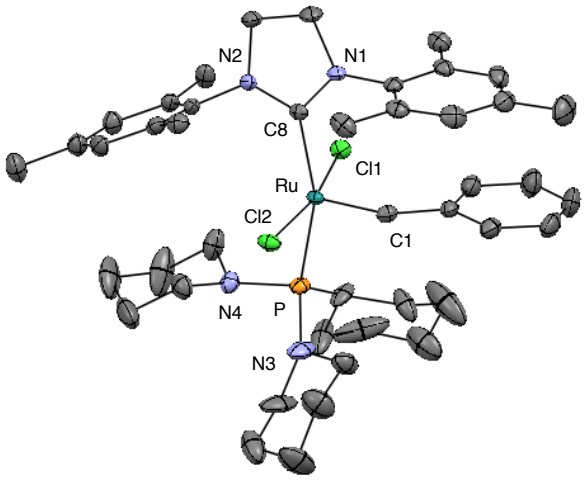

Figure 4.4. X-ray crystal structure of catalyst **4-8** with 50% probability ellipsoids. Hydrogen atoms have been omitted for clarity.

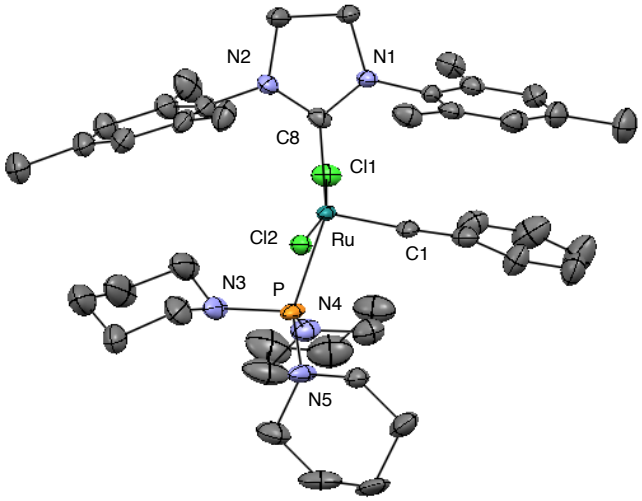

Figure 4.5. X-ray crystal structure of catalyst **4-9** with 50% probability ellipsoids. Hydrogen atoms have been omitted for clarity.

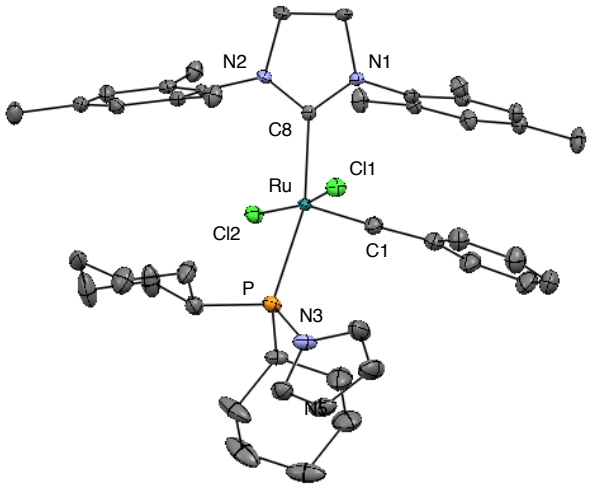

Figure 4.6. X-ray crystal structure of catalyst **4-17** with 50% probability ellipsoids. Hydrogen atoms have been omitted for clarity.

Table 4.2. Selected Bond Lengths and Angles for Complexes 4-2 and 4-7 through 4-9

bond lengths[a]	complex **4-2**	complex **4-7**	complex **4-8**	complex **4-9**
Ru–C1	1.835(2)	1.836(2)	1.839(3)	1.825(5)
Ru–C8	2.085(2)	2.0877(19)	2.097(3)	2.121(4)
Ru–P	2.4245(5)	2.4340(5)	2.3820(10)	2.394(3)
Ru–Cl1	2.3988(5)	2.4032(5)	2.3944(9)	2.374(5)
Ru–Cl2	2.3912(5)	2.3860(5)	2.4005(10)	2.421(3)
bond angles[b]	complex **4-2**	complex **4-7**	complex **4-8**	complex **4-9**
C1–Ru–C8	100.24(8)	99.70(8)	102.32(14)	102.1(2)
C1–Ru–P	95.89(6)	94.79(6)	100.29(11)	100.64(17)
C8–Ru–P	163.73(6)	165.40(6)	157.29(9)	157.17(14)

[a]Bond lengths reported in angstroms (Å). [b]Bond angles reported in degrees (º).

Kinetics Studies

The effect of P–N bonds on catalyst activity was first analyzed by comparing catalyst initiation rates for **4-4** through **4-9**. The rate constants of phosphine dissociation (k_1) for complexes **4-2** and **4-4** through **4-9** were measured at 30 °C in toluene-d_8 by ^{1}H NMR spectroscopy. These experiments allow for the comparison of two complete series

of new morpholinophosphine- (Figure 4.7) and piperidinophosphine-ligated (Figure 4.8) catalysts along with the known parent catalyst **4-2**. Initiation rate constants of the complexes were determined using a previously described method involving quenching with excess ethyl vinyl ether under pseudo-first-order conditions and monitoring the disappearance of the benzylidene resonance by ^{1}H NMR spectroscopy.[19a,23] Furthermore, the dissociation rates shown in Figures 4.7 and 4.8 are consistent with predicted values (within 10%) from kinetics experiments performed to compare the relative k_{-1} constants, or the rate of phosphine reassociation (*vide infra*). Under the same conditions, an experiment to determine the initiation rate of catalyst **4-17** resulted in full consumption of the benzylidene faster than the time scale to obtain a precise rate measurement. As expected, catalyst **4-17** is faster-initiating than all other complexes reported in this study containing morpholine and piperidine substituents; the lower limit of the initiation rate constant for this catalyst is $> 2 \times 10^{-2}$ s^{-1}. While the reaction kinetics of this complex are not included for the systematic study of amine incorporation, **4-17** was later tested in ROMP studies.

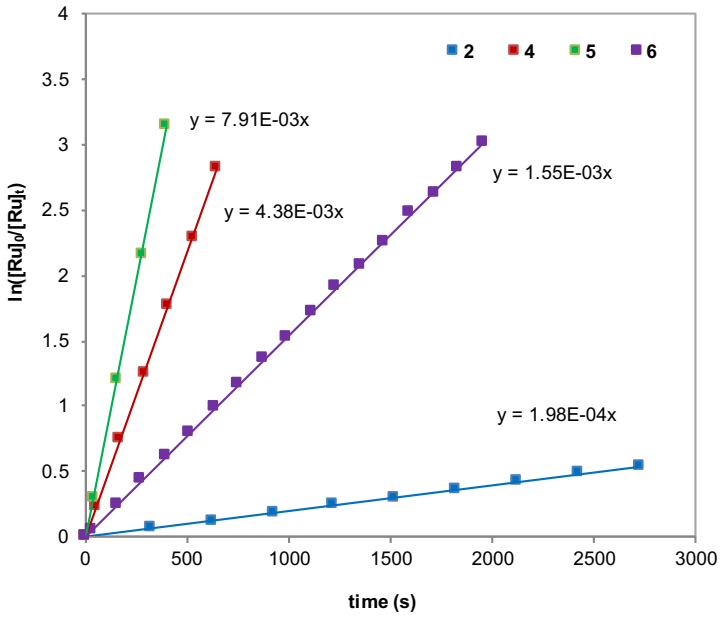

Figure 4.7. Initiation rates of catalyst series bearing morpholinophosphine ligands (catalysts **4-4** through **4-6**) and catalyst **4-2** determined by ^{1}H NMR spectroscopy at 30 °C with [Ru] = 0.017 M in toluene-d_8. The rates of phosphine dissociation are reported as the slopes of the lines fit to pseudo-first-order kinetics; units are (s^{-1}).

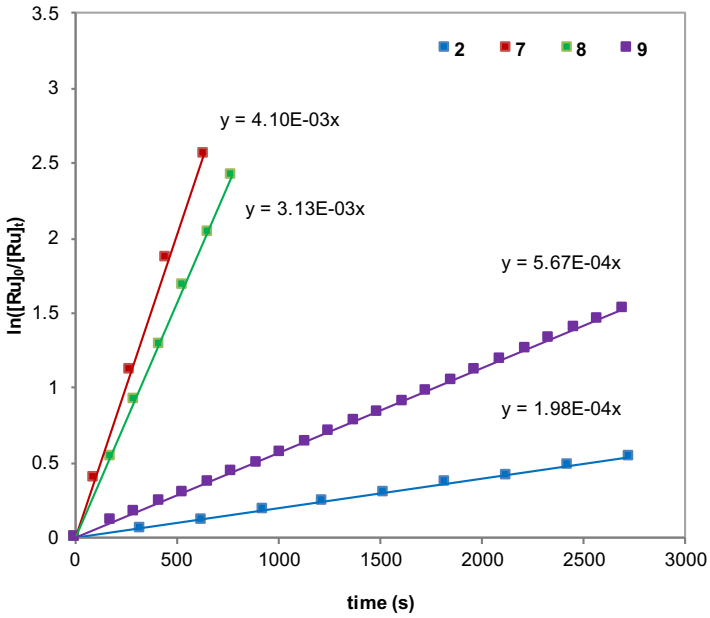

Figure 4.8. Initiation rates of catalyst series bearing morpholinophosphine ligands (catalysts **4-7** through **4-9**) and catalyst **4-2** determined by ^{1}H NMR spectroscopy at 30 °C with [Ru] = 0.017 M in toluene-d_8. The rates of phosphine dissociation are reported as the slopes of the lines fit to pseudo-first-order kinetics; units are (s^{-1}).

In all cases, the aminophosphine ligands dissociate at a faster rate than the PCy_3 ligand of catalyst **4-2**. In fact, complex **4-5,** containing a ligand with two morpholine substituents, initiates ~40 times faster than the parent catalyst and has the highest initiation rate of these two series. Interestingly, the tris(amino)phosphine-ligated complexes in both series appear to have anomalous reactivity. While amine substitution seems to dramatically accelerate phosphine dissociation for both mono-and bis(amino)phosphines relative to the PCy_3 ligand of catalyst **4-2**, this effect is somewhat muted for the tris(amino)phosphine-ligated complexes **4-6** and **4-9**, which are the slowest initiating complexes of each respective series. The initiation rates of catalysts **4-7** through **4-9**, although faster than that of catalyst **4-2**, decrease with increasing piperidine substitution (Figure 4.8). These data suggest that factors other than the anticipated inductive effects associated with amine incorporation significantly contribute to phosphine donor strength and dissociation rates. Further investigations of catalyst activity, including comparison of phosphine reassociation rates and DFT studies, were required to understand the observed trends in initiation rates.

In order to gain a more complete understanding of the effect of amine substitution on the strength of phosphine binding in second-generation ruthenium catalysts, we next performed experiments to compare the phosphine reassociation rate constants (k_{-1}) at 30 °C in toluene-d_8 by ^{1}H NMR spectroscopy. Following phosphine dissociation, the 14-electron intermediate, which is equivalent for all catalysts discussed in this study, can remain in the catalytic cycle and undergo olefin binding (k_2) or the phosphine can rebind to the metal (k_{-1}). Thus, the measurable ratio k_{-1}/k_2, determined from the slope of the line of best fit according to Equation 4.1,[24] represents the relative likelihood of these two events. Because phosphine dissociation leads to the same 14-electron intermediate in each case, the propagation rate k_2 is expected to be equivalent for catalysts **4-2** and **4-4** through **4-9**. For this reason, studies to determine k_{-1}/k_2 also allow for the comparison of phosphine reassociation rates (k_{-1}) across catalysts **4-4** through **4-9**.

$$1/k_{obs} = k_{-1}[\text{free aminophosphine}]/k_1k_2[\text{olefin}] + 1/k_1 \quad (4.1)$$

We applied our previously described procedure[19a] to determine relative phosphine reassociation rates to aminophosphine ligated catalysts, in order to evaluate the effect of P–N bonds on the propensity of these ligands to rebind to the ruthenium center. An example of the results of such an experiment, which incorporates a large excess of ethyl vinyl either and the free phosphine, for catalyst **4-2** is shown in Figure 4.9. The slope of the line of best fit is an estimate for the value of $k_{-1}/(k_1k_2)$, and the reciprocal of the y-intercept provides a predicted value of the initiation rate.

The estimated values of k_{-1}/k_2 for catalysts **4-2**, and **4-4** through **4-9** were determined at 30 ºC (Table 4.3). For the morpholinophophine series (**4-4** through **4-6**), the rate of phosphine reassociation directly correlates with amine substitution. As an increasing number of P–N bonds is systematically introduced into the ligand structure of catalyst **4-2**, a gradual increase in k_{-1} is observed in the case of morpholine substitution. However, this trend is not observed for the piperidinophophine series (**4-7** through **4-9**). Instead, the kinetics of phosphine reassociation are much less varied across this series, and all estimated values of k_{-1} are similar to that of the parent catalyst **4-2**.

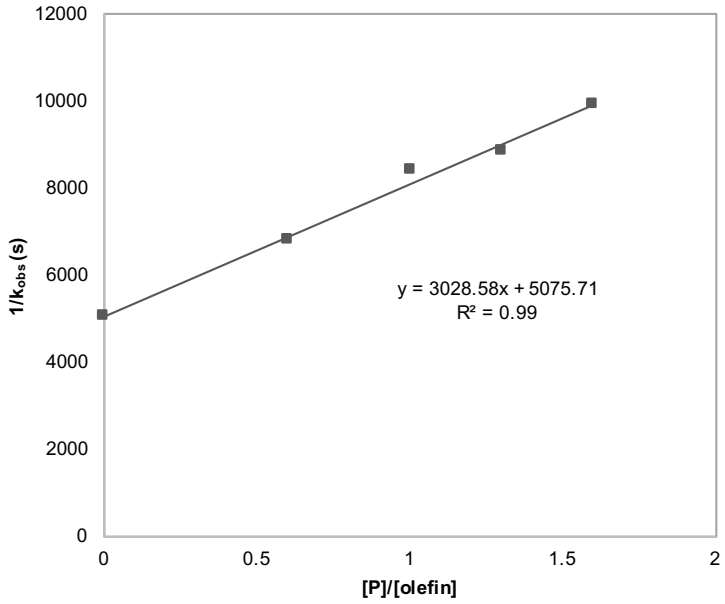

Figure 4.9. Example of $1/k_{obs}$ vs. [P]/[olefin] for catalyst **4-2** determined by ^{1}H NMR spectroscopy at 30 °C with [Ru] = 0.017 M in toluene-d_8.

Table 4.3. Estimated k_{-1}/k_2 Values for Catalysts 4-2 and 4-4 Through 4-9.[a]

catalyst	k_{-1}/k_2
4-2	0.60
4-4	1.44
4-5	1.82
4-6	3.00
4-7	0.70
4-8	0.57
4-9	0.71

[a]Measured using ^{1}H NMR spectroscopy at 30 °C with [Ru] = 0.017 M in toluene-d_8.

Discussion

The combined results from kinetics studies of complexes **4-4** through **4-9** were analyzed in detail to determine the effect of amine substituents on phosphine binding and to identify key factors that correlate to observed trends. The relative ratios of k_{-1} to k_1 were calculated for each complex, and this value k_{-1}/k_1 is used as a metric for ligand binding

strength. Thus, a stronger ligand is expected to have a higher k_{-1}/k_1, and these values provide an approximation of the relative phosphine binding constants. Normalized values for k_1, k_{-1}, and k_{-1}/k_1 are compared across each series **4-4** through **4-6** and **4-7** through **4-9** in Figure 4.10.

Increasing the number of morpholine substituents causes a steady increase in initiation rates when comparing catalysts **4-2**, **4-4**, and **4-5**. However, there is a break in trend for the tris(morpholino)phosphine, which dissociates at a significantly slower rate. In comparison, the incorporation of piperidine rings into the ligand composition of catalyst **4-2** leads to faster-initiating catalysts, but initiation rates decrease as more piperidine substituents are introduced. Despite these differences in trend, for both series, the tris(amino)phosphine ligated complexes **4-6** and **4-9** are clearly the slowest-initiating catalysts. As stated previously, the observed trend in k_{-1} for the morpholine series is not true for the piperidine series. These data suggest that k_{-1} constants do not correlate well with inductive effects related to phosphine composition.

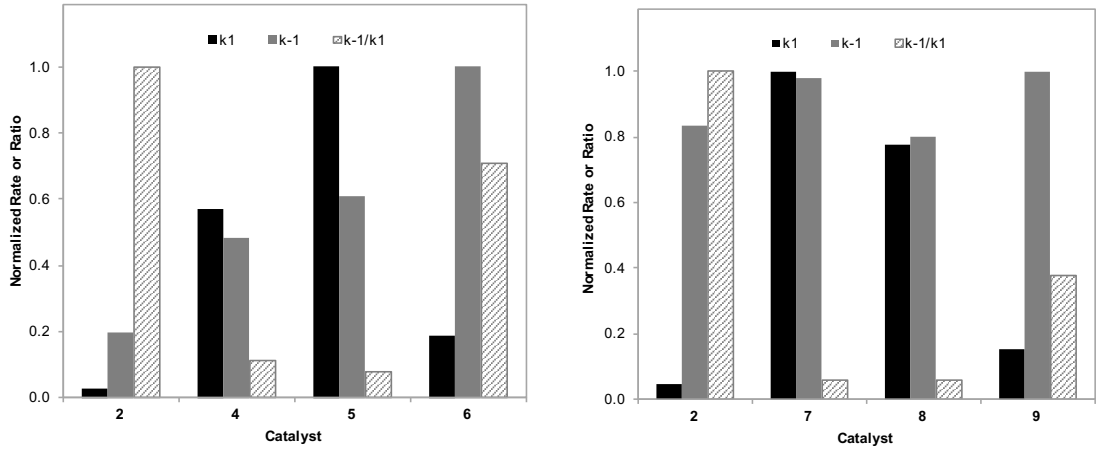

Figure 4.10. Comparisons of k_1, k_{-1}, and k_{-1}/k_1 for catalyst series bearing morpholinophosphine ligands (catalysts **4-4** through **4-6**) and piperidinophosphine ligands (catalysts **4-7** through **4-9**) as well as catalyst **4-2**. All values are normalized with respect to the highest value in each data set (denoted by shading).

The k_{-1}/k_1 ratios were compared and normalized with respect to that of catalyst **4-2**, which has a higher k_{-1}/k_1 and binding constant than catalysts **4-4** through **4-9**. Although the trends in phosphine dissociation and reassociation rates in the morpholine series differ

from those in the piperidine series, the overall trend in k_{-1}/k_1 are the same in both series of aminophosphine ligated catalysts. For both graphs shown in Figure 4.10, a U-shaped trend is observed for the phosphine binding constants as the number of P–N bonds increases from 0 (for catalyst **4-2**) to 3 (for catalysts **4-6** and **4-9**).

Computational studies were performed by collaborators[26] to gain insight into the underlying factors influencing the observed trends shown in Figure 4.10 and are briefly summarized below. These studies have confirmed that two favorable ligand conformations exist for mono- or bis(amino)phosphine ligands; the observed ligand geometry is dependent upon the nature of the substituents on the phosphine and its presence as a free or complexed ligand. In one case, a cyclohexyl ring sits in a pseudo-equatorial position, which is observed in the crystal structure of catalyst **4-7**, confirming the orientation of this cyclohexyl ring away from the benzylidene and under a mesityl group of the NHC (Figure 4.3). In the other case, an amine group is in the pseudo-equatorial position, and this ligand conformation is confirmed in the crystal structure of catalyst **4-8**, which shows a piperidine ring in this position oriented away from the benzylidene (Figure 4.4). The DFT-optimized geometries suggest that trends in phosphine dissociation energy are the result of a combination of steric effects (notably those involving the pseudo-equatorial phosphine substituent and the NHC mesityl), inductive effects (derived from the increased electronegativity of nitrogen compared to carbon), orbital overlap of the nitrogen (amine) lone pair with the Ru–P σ^* orbital, and ligand distortion energy. Computed pKa and Tolman Electronic Parameter values are in agreement with observed trends in phosphine binding constants. Furthermore, modeling of the phosphine dissociation reaction coordinate suggests that differences in ligand conformation of the catalyst ground state and transition state can have a significant influence in accelerating initiation rates.

Applications to Ring-Opening Metathesis Polymerization

The catalysts were next evaluated in ROMP, and the reaction kinetics as well as dispersities of the resulting polymers were compared. The substituted norbornene **4-18** was selected as a model monomer[25] to distinguish the catalytic activities of piperidinophosphine-ligated complexes **4-7** through **4-9** from those of catalysts **4-2** and **4-**

3, and to identify potential correlations with the previously determined rate constants (Figure 4.11). Catalyst **4-3** is known to be an efficient and effective ROMP catalyst, while use of the parent catalyst **4-2** can lead to uncontrolled molecular weights and broad molecular weight distributions.[15] Furthermore, the activity of the fast-initiating catalyst **4-17** containing a pyrrole was evaluated.

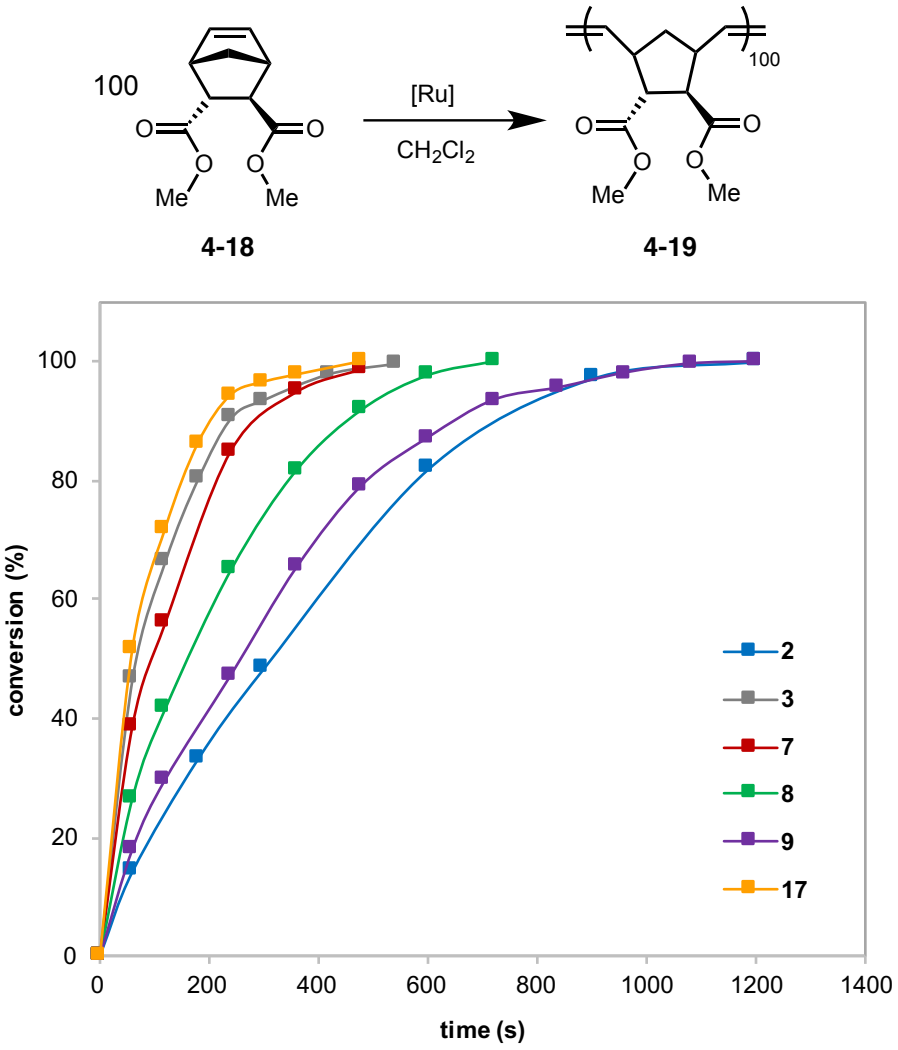

Figure 4.11. Reaction profiles of aminophosphine-ligated complexes **4-7** through **4-9** and **4-17** compared to known catalysts **4-2** and **4-3**.

The ROMP of **4-18** was performed in DCM at 30 ºC and monomer conversion was monitored by size-exclusion chromatography (SEC) and ^{1}H NMR spectroscopy. All tested aminophosphine-ligated complexes had higher rates of polymerization than the parent catalyst **4-2**, which showed the lowest rate of conversion and broadest molecular weight

distribution. For the piperidine catalyst series **4-7** through **4-9**, the rates of polymerization directly correlate with the initiation rates; while amine substitution causes an increase in the rate relative to **4-2**, the rate of polymerization increases as the number of P–N bonds (*n*) decreases, provided $n > 0$. The dispersities of the resulting polymers follow a similar trend, with catalyst **4-7** leading to narrower molecular weight distribution in comparison to **4-9**. Furthermore, although none of the catalysts in this series prove to be as efficient as **4-3** in the ROMP of **4-18**, polymerization with the fast-initiating pyrrolylphosphine-ligated catalyst **4-17** proceeded with a rate of conversion slightly higher than that of **4-3**, with similarly low polydispersity (1.03). Through the application of aminophosphine ligands, a simple change to a substituent in the phosphine in **4-2** results in the formation of much more efficient ROMP catalysts with reaction kinetics comparable to **4-3**. Studies of phosphines containing P–X bonds can aide in the design of new catalysts to broaden the scope of suitable monomer classes.

Conclusion

A new class of olefin metathesis catalysts, based on the incorporation of P–N bonds in the phosphine ligand of second-generation ruthenium complex **4-2**, was synthesized. Following facile synthesis of the aminophosphine ligands from morpholine and piperidine, the catalysts were formed in one step from complex **4-3**. The initiation rate and relative phosphine reassociation rate constants were determined, allowing for the comparison of aminophosphine ligand binding strengths. The results of kinetics studies and computational studies reveal that a combination of steric, inductive, and ligand conformational effects contribute to the observed trends in phosphine binding. Furthermore, DFT calculations suggest that ligand conformational changes in the transition state of the phosphine dissociation reaction coordinate are responsible for accelerated catalyst initiation rates. Finally, the application of the aminophosphine-ligated catalysts to ROMP demonstrates that simple changes to the substituents on the phosphine ligand can lead to a dramatic enhancement in catalyst reactivity. Investigations of novel phosphine classes, notably those containing incongruent substituents and P–X bonds, will facilitate catalyst modification and expand applications of metathesis to new olefin substrates.

Experimental Section

General Information

Solvents were dried by passing through an activated alumina column (*n*-pentane, benzene, toluene, Et_2O, and THF). Deuterated solvents were purchased from Cambridge Isotopes Laboratories, Inc. and were degassed and stored over activated 3 Å molecular sieves prior to use. C_6D_6 was purified by passage through a solvent purification column. Ethyl vinyl ether was degassed with argon or nitrogen gas prior to use. Catalyst **4-2** was obtained from Materia, Inc. The bispyridine complex **4-3** was synthesized according to literature procedure.[16] All reactions were carried out in dry glassware under an N_2 atmosphere unless otherwise indicated.

NMR spectra were measured with Varian 500 MHz, Varian 400 MHz, and Bruker 400 MHz spectrometers. High-resolution mass spectra (HRMS) were provided by the California Institute of Technology Mass Spectrometry Facility using a JEOL JMS-600H High Resolution Mass Spectrometer.

SEC data were collected using two Agilent PLgel MIXED-B 300 × 7.5 mm columns with 10 μm beads, connected to an Agilent 1260 Series pump, a Wyatt 18-angle DAWN HELEOS light scattering detector, and Optilab rEX differential refractive index detector. The mobile phase was THF.

The crystallographic measurements were performed at 100(2) K using a Bruker APEX–II CCD area detector diffractometer (Mo-K_α radiation, λ = 0.71073 Å). In each case, a specimen of suitable size and quality was selected and mounted onto a nylon loop. The structures were solved by direct methods, which successfully located most of the non-hydrogen atoms. Semi-empirical absorption corrections were applied. Subsequent refinement on F^2 using the SHELXTL/PC package (version 6.1) allowed location of the remaining non-hydrogen atoms.

Synthesis and Characterization of Aminophosphine-Ligated Complexes

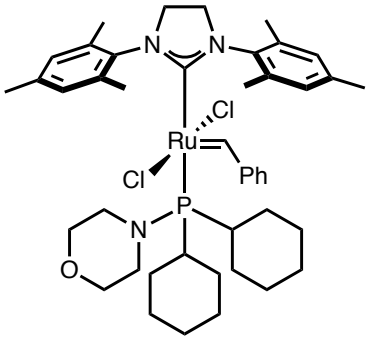

Catalyst 4-4. To a THF solution (2 mL) of the bispyridine complex **4-3** (150 mg, 0.206 mmol), was added 2.5 equivalent (146 mg, 0.516 mmol) of the appropriate phosphine ligand, 4-(dicyclohexylphosphanyl)morpholine in THF (1 mL). The resulting mixture was stirred at room temperature for 20 min. All volatiles were then removed under reduced pressure. Addition of pentane led to the formation of a pink precipitate of the desired complex, **4-4,** which was isolated by filtration through celite and dried under vacuum (129 mg, 73%). Dark brown crystals were obtained by slow Et_2O vapor diffusion into a THF solution of the title complex.

^{1}H NMR (500 MHz; C_7D_8): δ 19.51 (s, 1H), 9.14 (bs, 1H), 7.18 – 7.10 (m, 2H), 6.98 – 6.83 (m, 4H), 6.23 (bs, 2H), 3.61 – 3.17 (m, 9H), 2.76 (s, 6H), 2.65 – 2.25 (m, 10H), 2.21 (s, 3H), 1.79 (s, 3H), 1.70 – 1.39 (m, 11H), 1.23 – 0.98 (m, 8H), 0.76 (d, J = 12.5 Hz, 2H).

^{13}C NMR (101 MHz; C_6D_6): δ 296.25, 220.71 (d, $^2J_{C\text{-}P}$ = 84.8 Hz), 151.99, 139.39, 138.61, 137.63, 137.23, 135.59, 130.31, 129.39, 68.02, 52.11, 51.08, 49.37, 35.39 (d, $J_{C\text{-}P}$ = 19.6 Hz), 29.18, 28.74, 28.02, 27.93, 27.84, 27.72, 26.59, 21.23, 21.03, 20.57, 19.00.

^{31}P{^{1}H} NMR (162 MHz; C_6D_6): δ 92.4 (s).

MS (FAB) *m/z* (M^++H) calcd for $C_{44}H_{63}ON_3RuPCl_2$: 852.3130, found: 852.3153.

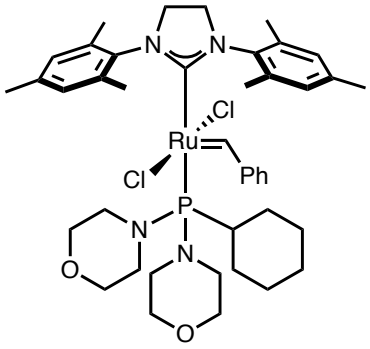

Catalyst 4-5. To a THF solution (2 mL) of the bispyridine complex **4-3** (100 mg, 0.138 mmol), was added 1.2 equivalent (47 mg, 0.165 mmol) of the appropriate phosphine ligand, 4,4'-(cyclohexylphosphanediyl)dimorpholine in THF (1 mL). The resulting mixture was stirred at room temperature for 20 min. All volatiles were then removed under reduced pressure. Addition of pentane led to the formation of a pink precipitate of the desired complex, **4-5,** which was isolated by filtration through celite and dried under vacuum (79 mg, 67%).

^{1}H NMR (400 MHz; C_6D_6): δ 19.40 (s, 1H), 8.17 (bs, 2H), 7.12 (t, J = 7.6 Hz, 1H), 7.06 (s, 2H), 6.93 (t, J = 7.6 Hz, 2H), 6.21 (bs, 2H), 3.50 – 3.21 (m, 12H), 3.09 (t, J = 12.3 Hz, 1H), 2.86 (bs, 9H), 2.66 – 2.40 (m, 13H), 1.79 (s, 3H), 1.67 – 1.51 (m, 6H), 1.17 – 1.10 (m, 2H), 0.99 (tt, J = 12.6 Hz, J = 3.5 Hz, 1H), 0.77 (q, J = 12.4 Hz, 2H).

^{13}C NMR (101 MHz; C_6D_6): δ 293.55, 221.10 (d, $^{2}J_{C\text{-}P}$ = 89.0 Hz), 151.59, 139.44, 139.26, 137.69, 137.49, 136.93, 135.03, 131.06, 130.55, 129.37, 67.64, 52.14, 50.97, 47.16, 37.38 (d, $J_{C\text{-}P}$ = 23.7 Hz), 27.66, 27.48, 27.36, 27.25, 21.23, 21.00, 20.63, 18.92.

^{31}P{^{1}H} NMR (161.8 MHz; C_6D_6): δ 131.9 (s).

MS (FAB) *m/z* (M^+) calcd for $C_{42}H_{59}O_2N_4RuPCl_2$: 854.2797, found: 854.2834.

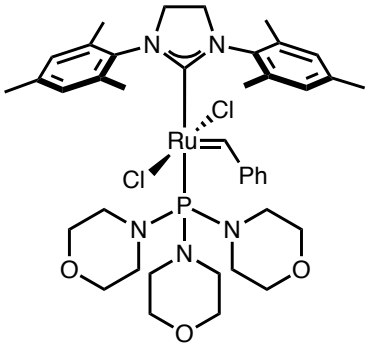

Catalyst 4-6. To a THF solution (2 mL) of the bispyridine complex **4-3** (173 mg, 0.238 mmol), was added 1.2 equivalent (82 mg, 0.286 mmol) of the appropriate phosphine ligand, trimorpholinophosphane in THF (1 mL). The resulting mixture was stirred at room temperature for 20 min. All volatiles were then removed under reduced pressure. Addition of pentane led to the formation of a pink precipitate of the desired complex, **4-6,** which was isolated by filtration through celite and dried under vacuum (157 mg, 77%).

^{1}H NMR (500 MHz; C_7D_8): δ 19.44 (s, 1H), 8.03 (s, 2H), 7.12 (s, 1H), 6.93 – 6.85 (m, 4H), 6.16 (s, 2H), 3.46 – 3.37 (m, 2H), 3.33 – 3.21 (m, 14H), 2.75 (s, 6H), 2.68 (q, J = 4.7 Hz, 12H), 2.35 (s, 6H), 2.28 (s, 3H), 1.77 (s, 3H).

^{13}C NMR (101 MHz; C_6D_6): δ 298.46, 219.58 (d, $^{2}J_{C\text{-}P}$ = 107.3 Hz), 151.81, 139.51, 139.07, 137.61, 137.52, 137.09, 135.33, 130.95, 130.24, 129.40, 128.80, 128.59, 67.60 (d, $J_{C\text{-}P}$ = 5.8 Hz), 51.90 (d, $J_{C\text{-}P}$ = 4.7 Hz), 50.91 (d, $J_{C\text{-}P}$ = 2.9 Hz), 46.86 (d, $J_{C\text{-}P}$ = 3.0 Hz), 21.14, 20.97, 20.65, 18.92.

^{31}P{^{1}H} NMR (162 MHz; C_6D_6): δ 116.7 (s).

MS (FAB) *m/z* (M^+) calcd for $C_{40}H_{56}O_3N_5RuPCl_2$: 857.2542, found: 857.2517.

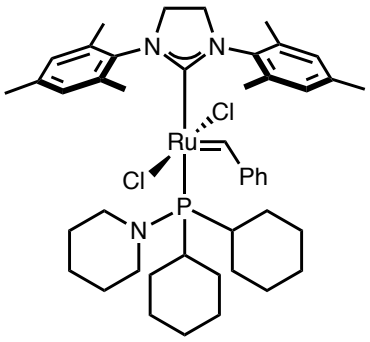

Catalyst 4-7. To a THF solution (2 mL) of the bispyridine complex **4-3** (100 mg, 0.138 mmol), was added 1.2 equivalent (46.5 mg, 0.165 mmol) of the appropriate phosphine ligand,

1-(dicyclohexylphosphanyl)piperidine in THF (1 mL). The resulting mixture was stirred at room temperature for 20 min. All volatiles were then removed under reduced pressure. Addition of pentane led to the formation of a pink precipitate of the desired complex, **4-7,** which was isolated by filtration through celite and dried under vacuum (93 mg, 80%). Dark brown crystals were obtained by slow Et_2O vapor diffusion into a benzene solution of the title complex.

^{1}H NMR (400 MHz; C_6D_6): δ 19.70 (s, 1H), 9.37 (bs, 1H), 7.19 – 7.12 (m, 2H), 7.06 – 6.89 (m, 4H), 6.80 – 5.56 (m, 2H), 3.50 – 3.14 (m, 5H), 3.08 – 2.75 (m, 7H), 2.73 – 2.55 (m, 7H), 2.21 (s, 3H), 1.82 (s, 3H), 1.79 – 1.04 (m, 26H), 0.95 – 0.77 (m, 2H).

^{13}C NMR (101 MHz; C_6D_6): δ 296.05, 221.10 (d, $^2J_{C\text{-}P}$ = 83.5 Hz), 152.07, 139.43, 138.29, 137.75, 137.54, 137.27, 135.87, 130.29, 129.39, 128.30, 128.06, 127.82, 52.19, 51.10, 50.31, 35.88 (d, $J_{C\text{-}P}$ = 19.9 Hz), 29.31, 28.86, 28.12, 28.03, 27.94, 27.81, 27.45, 27.40, 26.68, 25.18, 21.14 (d, $J_{C\text{-}P}$ = 18.0 Hz), 20.60, 19.07.

^{31}P{^{1}H} NMR (161.8 MHz; C_6D_6): δ 92.1 (s).

MS (FAB) *m/z* (M^+) calcd for $C_{45}H_{64}N_3RuPCl_2$: 849.3259, found: 849.3267.

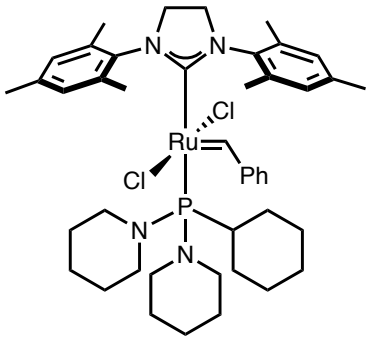

Catalyst 4-8. To a THF solution (2 mL) of the bispyridine complex **4-3** (130 mg, 0.179 mmol), was added 1.2 equivalent (210 mg, 0.744 mmol) of the appropriate phosphine ligand, 1,1'-(cyclohexylphosphanediyl)dipiperidine in THF (1 mL). The resulting mixture was stirred at room temperature for 20 min. All volatiles were then removed under reduced pressure. Addition of pentane led to the formation of a pink precipitate of the desired complex, **4-8,** which was isolated by filtration through celite and dried under vacuum (82 mg, 54%). Dark brown crystals were obtained by slow Et_2O vapor diffusion into a THF solution of the title complex.

^{1}H NMR (400 MHz; C_6D_6): δ 19.47 (s, 1H), 8.46 (bs, 1H), 7.19 – 7.13 (m, 2H), 7.01 (t, J = 7.7 Hz, 2H), 6.94 (s, 2H), 6.77 – 5.44 (m, 2H), 3.44 – 3.17 (m, 4H), 3.04 – 2.75 (m, 11H), 2.75 – 2.56 (s, 6H), 2.22 (s, 3H), 1.82 (s, 3H), 1.69 – 1.50 (m, 5H), 1.41 (s, 11H), 1.28 (s, 7H), 1.08 – 0.75 (m, 3H).

^{13}C NMR (101 MHz; C_6D_6): δ 291.90, 222.33 (d, $^{2}J_{C\text{-}P}$ = 87.8 Hz), 151.79, 139.65, 138.08, 137.96, 137.35, 136.97, 135.91, 131.17, 130.35, 129.36, 128.30, 128.06, 127.82, 52.34, 52.30, 50.97, 47.68, 38.15 (d, $J_{C\text{-}P}$ = 23.9 Hz), 27.80, 27.63, 27.50, 27.16, 27.11, 25.77, 25.22, 21.12 (d, $J_{C\text{-}P}$ = 12.9 Hz), 20.64, 19.07.

^{31}P{^{1}H} NMR (161.8 MHz; C_6D_6): δ 133.0 (s).

MS (FAB) *m/z* (M^+) calcd for $C_{44}H_{63}N_4RuPCl_2$: 850.3211, found: 850.3212.

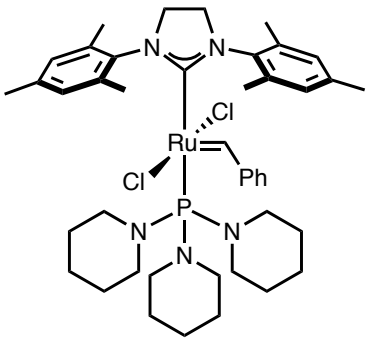

Catalyst 4-9. To a THF solution (2 mL) of the bispyridine complex **4-3** (100 mg, 0.138 mmol), was added 1.5 equivalent (58.7 mg, 0.207 mmol) of the appropriate phosphine ligand, tri(piperidin-1-yl)phosphane in THF (1 mL). The resulting mixture was stirred at room temperature for 20 min. All volatiles were then removed under reduced pressure. Addition of pentane led to the formation of a pink precipitate of the desired complex, **4-9,** which was isolated by filtration through celite and dried under vacuum (92 mg, 78%). Dark brown crystals were obtained by slow pentane vapor diffusion into a THF solution of the title complex.

^{1}H NMR (400 MHz; C_6D_6): δ 19.70 (s, 1H), 8.30 (bs, 2H), 7.21 – 7.17 (m, 1H), 7.04 – 6.98 (m, 2H), 6.93 (s, 2H), 6.25 (s, 2H), 3.43 – 3.16 (m, 4H), 2.86 (s, 6H), 2.85 – 2.77 (m, 12H), 2.48 (s, 6H), 2.22 (s, 3H), 1.82 (s, 3H), 1.48 – 1.34 (m, 6H), 1.29 (m, 12H).

^{13}C NMR (101 MHz; C_6D_6): δ 296.09, 221.30 (d, $^{2}J_{C\text{-}P}$ = 105.2 Hz), 152.12, 139.67, 138.04, 137.89, 137.38, 137.17, 136.04, 131.22, 130.18, 129.37, 52.07 (d, $J_{C\text{-}P}$ = 4.9 Hz),

50.94, 47.19 (d, $J_{C\text{-}P}$ = 4.4 Hz), 27.08 (d, $J_{C\text{-}P}$ = 4.6 Hz), 25.70, 21.09 (d, $J_{C\text{-}P}$ = 10.4 Hz), 20.72, 19.10.

$^{31}P\{^{1}H\}$ NMR (161.8 MHz; C_6D_6): δ 118.7 (s).

MS (FAB) *m/z* (M^+) calcd for $C_{43}H_{62}N_5RuPCl_2$: 851.3164, found: 851.3178.

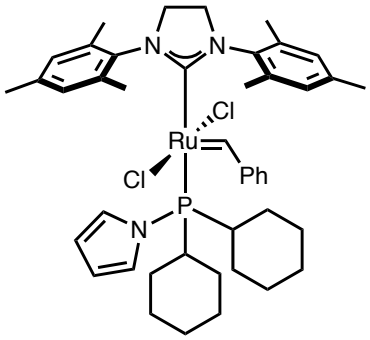

Catalyst 4-17. To a THF solution (2 mL) of the bispyridine complex **4-3** (100 mg, 0.138 mmol), was added 2.0 equivalent (73 mg, 0.275 mmol) of the appropriate phosphine ligand, 1-(dicyclohexylphosphanyl)-1*H*-pyrrole in THF (1 mL). The resulting mixture was stirred at room temperature for 20 min. All volatiles were then removed under reduced pressure. Addition of pentane led to the formation of a pink precipitate of the desired complex, **4-17,** which was isolated by filtration through celite and dried under vacuum (110 mg, 96%). Dark brown crystals were obtained by slow pentane vapor diffusion into a THF solution of the title complex.

^{1}H NMR (400 MHz; C_6D_6): δ 19.82 (s, 1H), 8.24 (bs, 2H), 7.10 (t, *J* = 7.2 Hz, 1H), 6.94 – 6.90 (m, 4H), 6.74 (q, *J* = 2.2 Hz, 2H), 6.21 (s, 4H), 3.36 (dt, *J* = 2.3 Hz, *J* = 10.6 Hz, 2H), 3.23 (dt, *J* = 2.3 Hz, *J* = 10.6 Hz, 2H), 2.81 (s, 6H), 2.44 (s, 6H), 2.19 (s, 3H), 1.80 (s, 3H), 1.63 (d, *J* = 10.8 Hz, 2H), 1.54 (d, *J* = 11.0 Hz, 2H), 1.46 – 1.35 (m, 6H), 1.27 (qt, *J* = 12.7 Hz, *J* = 3.4 Hz, 2H), 1.12 – 0.91 (m, 6H), 0.52 (qt, *J* = 12.7 Hz, *J* = 3.4 Hz, 2H).

^{13}C NMR (101 MHz; C_6D_6): δ 301.30, 219.39 (d, $^{2}J_{C\text{-}P}$ = 89.9 Hz), 151.99, 139.40, 138.57, 137.86, 137.37, 137.25, 135.47, 131.50, 130.28, 129.44, 128.97, 128.59, 125.32 (d, $J_{C\text{-}P}$ = 2.8 Hz), 110.26 (d, $J_{C\text{-}P}$ = 4.6 Hz), 52.09 (d, $J_{C\text{-}P}$ = 4.1 Hz), 51.11 (d, $J_{C\text{-}P}$ = 2.1 Hz), 35.81 (d, $J_{C\text{-}P}$ = 18.6 Hz), 28.30 (d, $J_{C\text{-}P}$ = 4.3 Hz), 27.85 (d, $J_{C\text{-}P}$ = 2.8 Hz), 27.53, 27.44, 27.40, 27.27, 25.99, 21.25, 21.01, 20.58, 18.95.

$^{31}P\{^{1}H\}$ NMR (162 MHz; C_6D_6): δ 92.3 (s).

MS (FAB) *m/z* (M^+) calcd for $C_{44}H_{58}N_3RuPCl_2$: 831.2789, found: 831.2761.

Initiation Rate Studies

The ruthenium benzylidene complex was dissolved in toluene-d_8 (600 μL, 0.017 M) in an NMR tube fitted with a septum cap sealed under an N_2 atmosphere. To this NMR tube was injected neat ethyl vinyl ether (30 equiv.) using a micro-syringe under inert atmosphere. The tube was inverted and immediately loaded into a 500 MHz ^{1}H NMR spectrometer pre-warmed to 30 °C, at which point the first-order depletion of the benzylidene Ru=C*H*Ph signal was monitored.

Estimation of k_{-1}/k_2

A solution of toluene-d_8 (600 μL) containing the ruthenium benzylidene complex (0.017 M) and free aminophosphine ([P]/[ethyl vinyl ether] = 0.6, 1.0, 1.6) was added to an NMR tube fitted with a septum cap and sealed under an N_2 atmosphere. To this NMR tube was injected neat ethyl vinyl ether (15 μL) using a micro-syringe under inert atmosphere. The tube was inverted and immediately loaded into a 500 MHz ^{1}H NMR spectrometer pre-warmed to 30 °C, at which point the first-order depletion of the benzylidene Ru=C*H*Ph signal was monitored. The values of $1/k_{obs}$ were plotted vs. [P]/[ethyl vinyl ether], including the data from initiation rate studies where [P]/[olefin] = 0. The graph for each catalyst is shown below. The ratio of k_{-1}/k_2 was calculated by dividing the slope of the line of best fit by the y-intercept.

Catalyst 4-4

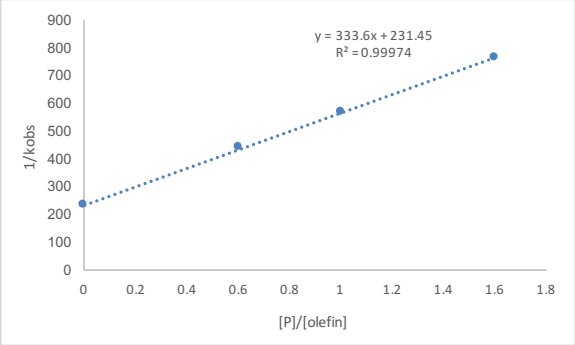

Catalyst 4-5

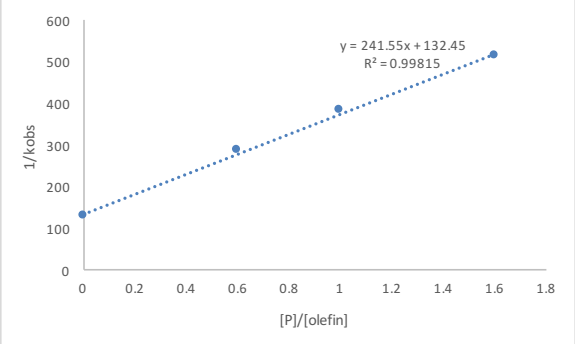

Catalyst 4-6

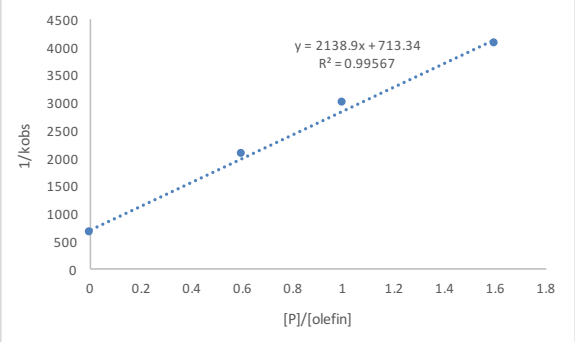

Catalyst 4-7

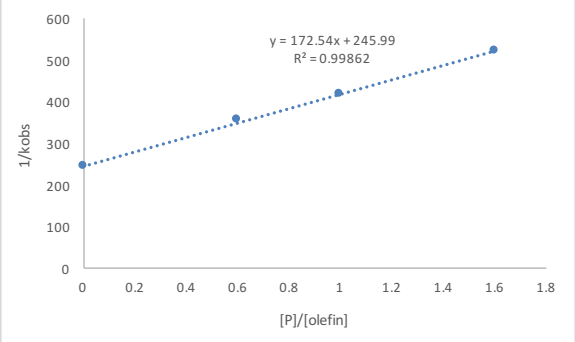

Catalyst 4-8

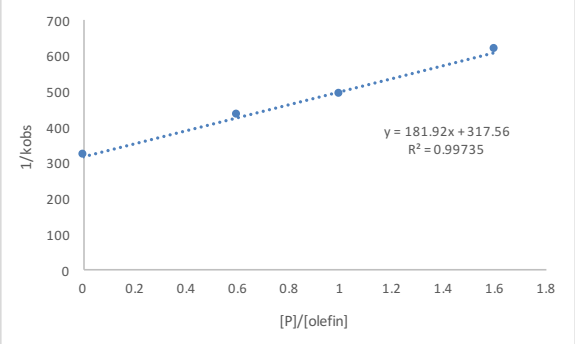

Catalyst 4-9

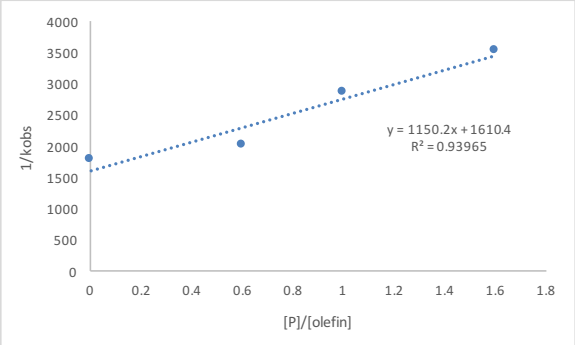

Evaluation of Selected Catalysts in ROMP

A solution of **4-18** (21.0 mg, 0.100 mmol) was prepared in 2 mL of dichloromethane at 298 K. While stirring, the polymerization was initiated by addition of a CH_2Cl_2 solution of catalyst (0.0500 M, 20.0 µL, 0.100 µmol). During the course of the reaction, aliquots (~50 µL) were extracted and quenched in separate vials containing a large excess of ethyl vinyl ether (0.1 mL) in THF (0.9 mL). The quenched reaction mixtures were analyzed by SEC and ^{1}H NMR spectroscopy to determine norbornene conversion, molecular weight (M_n), and dispersity ($Đ$).

Table 4.4. Molecular Weights and Dispersities of Polymers 4-19.

Catalyst	M_n (kDa)	*Đ*
4-3	23.1	1.02
4-2	96.1	1.50
4-7	46.3	1.17
4-8	55.2	1.22
4-9	70.1	1.41
4-17	25.9	1.03

Crystallographic Data

Table 4.5. Crystal Data and Structure Analysis Details for Catalyst 4-7.
(Structure shown in Figure 4.3)

Empirical formula	C100 H144 Cl4 N6 O P2 Ru2	
Formula weight	1852.08	
Crystal shape	block	
Crystal color	brown	
Crystal size	0.050 x 0.080 x 0.100 mm^3	
Data Collection		
Preliminary photograph(s)	rotation	
Type of diffractometer	CCD area detector	
Wavelength	0.71073 Å	
Data collection temperature	100(2) K	
Theta range for 9838 reflections used		
in lattice determination	4.655 to 65.411º	
Unit cell dimensions	a = 12.5478(5) Å	α= 90º
	b = 14.1495(6) Å	β= 92.828(2)º
	c = 26.7547(11) Å	γ = 90º
Volume	4744.4(3) $Å^3$	
Z	2	
Crystal system	monoclinic	

Space group	P $2_1/c$
Density (calculated)	1.296 g/cm^3
F(000)	1960
Theta range for data collection	1.6 to 37.7º
Completeness to theta = 25.242º	100.0%
Index ranges	$-21 \leq h \leq 21$, $-24 \leq k \leq 23$, $-45 \leq l \leq 45$
Reflections collected	180275
Independent reflections	24676 [R_{int}= 0.0782]
Reflections > 2s(I)	17555
Average s(I)/(net I)	0.0619
Absorption coefficient	0.51 mm^{-1}
Absorption correction	Semi-empirical from equivalents
Max. and min. transmission	0.6876 and 0.6876
Structure Solution and Refinement	
Hydrogen placement	geom
Refinement method	Full-matrix least-squares on F^2
Data / restraints / parameters	24676 / 17 / 520
Treatment of hydrogen atoms	constr
Goodness-of-fit on F^2	1.07
Final R indices [I>2s(I), 17555 reflections]	R1 = 0.0561, *w*R2 = 0.1214
R indices (all data)	R1 = 0.0959, *w*R2 = 0.1363
Type of weighting scheme used	calc
Max shift/error	0.001
Average shift/error	0.000
Extinction coefficient	n/a
Largest diff. peak and hole	2.49 and -1.63 e/Å^{-3}
Programs Used	
Structure refinement	SHELXL-2013 (Sheldrick, 2013)

Table 4.6. Crystal Data and Structure Analysis Details for Catalyst 4-8.
(Structure shown in Figure 4.4)

Empirical formula	C100 H152 Cl4 N8 O3 P2 Ru2 Si0	
Formula weight	1920.17	
Crystal shape	block	
Crystal color	brown	
Crystal size	0.020 x 0.150 x 0.150 mm^3	
Data Collection		
Preliminary photograph(s)	rotation	
Type of diffractometer	CCD area detector	
Wavelength	0.71073 Å	
Data collection temperature	100(2) K	
Theta range for 9872 reflections used		
in lattice determination	4.877 to 60.270º	
Unit cell dimensions	a = 12.582(4) Å	α= 90º
	b = 14.694(4) Å	β= 102.711(9)º
	c = 26.929(9) Å	γ = 90º
Volume	4856(3) $Å^3$	
Z	2	
Crystal system	monoclinic	
Space group	P $2_1/n$	
Density (calculated)	1.313 g/cm^3	
F(000)	2036	
Theta range for data collection	2.1 to 31.3º	
Completeness to theta = 25.242º	99.9%	
Index ranges	$-18 \le h \le 17$, $-21 \le k \le 21$, $-39 \le l \le 39$	
Reflections collected	109331	
Independent reflections	14689 [R_{int}= 0.0561]	
Reflections > 2s(I)	10910	
Average s(I)/(net I)	0.0580	

Absorption coefficient	0.51 mm^{-1}
Absorption correction	Semi-empirical from equivalents
Max. and min. transmission	1.0000 and 0.9533
Structure Solution and Refinement	
Hydrogen placement	geom
Refinement method	Full-matrix least-squares on F^2
Data / restraints / parameters	14689 / 2 / 538
Treatment of hydrogen atoms	constr
Goodness-of-fit on F^2	1.04
Final R indices [I>2s(I), 10910 reflections]	R1 = 0.0645, *w*R2 = 0.1465
R indices (all data)	R1 = 0.1013, *w*R2 = 0.1643
Type of weighting scheme used	calc
Max shift/error	0.001
Average shift/error	0.000
Extinction coefficient	n/a
Largest diff. peak and hole	2.26 and -1.25 e/$Å^{-3}$
Programs Used	
Structure refinement	SHELXL-2013 (Sheldrick, 2013)

Table 4.7. Crystal Data and Structure Analysis Details for Catalyst 4-9.
(Structure shown in Figure 4.5)

Empirical formula	C43 H62 Cl2 N5 P Ru
Formula weight	851.91
Crystal shape	block
Crystal color	brown
Crystal size	0.030 x 0.120 x 0.140 mm^3
Data Collection	
Preliminary photograph(s)	rotation
Type of diffractometer	CCD area detector
Wavelength	0.71073 Å

Data collection temperature	100(2) K	
Theta range for 9656 reflections used		
in lattice determination	5.207 to 62.321º	
Unit cell dimensions	a = 12.685(4) Å	α= 90º
	b = 14.502(4) Å	β= 99.043(12)º
	c = 22.983(7) Å	γ = 90º
Volume	4176(2) $Å^3$	
Z	4	
Crystal system	monoclinic	
Space group	P $2_1/c$	
Density (calculated)	1.355 g/cm^3	
F(000)	1792	
Theta range for data collection	2.3 to 33.6º	
Completeness to theta = 25.000º	99.9%	
Index ranges	$-18 \le h \le 19$, $-22 \le k \le 22$, $-34 \le l \le 30$	
Reflections collected	100488	
Independent reflections	15279 [R_{int}= 0.0733]	
Reflections > 2s(I)	10188	
Average s(I)/(net I)	0.0882	
Absorption coefficient	0.58 mm^{-1}	
Absorption correction	Semi-empirical from equivalents	
Max. and min. transmission	0.9954 and 0.9389	
Structure Solution and Refinement		
Hydrogen placement	geom	
Refinement method	Full-matrix least-squares on F^2	
Data / restraints / parameters	15279 / 138 / 704	
Treatment of hydrogen atoms	constr	
Goodness-of-fit on F^2	1.16	
Final R indices [I>2s(I), 10188 reflections]	R1 = 0.0820, *w*R2 = 0.1464	
R indices (all data)	R1 = 0.1400, *w*R2 = 0.1609	
Type of weighting scheme used	calc	

Max shift/error	0.001
Average shift/error	0.000
Extinction coefficient	n/a
Largest diff. peak and hole	1.13 and -1.50 e/Å^{-3}
Programs Used	
Structure refinement	SHELXL-2013 (Sheldrick, 2013)

Table 4.8. Crystal Data and Structure Analysis Details for Catalyst 4-17.
(Structure shown in Figure 4.6)

Empirical formula	C44 H58 Cl2 N3 P Ru	
Formula weight	831.87	
Crystal shape	block	
Crystal color	brown	
Crystal size	0.050 x 0.090 x 0.100 mm^3	
Data Collection		
Preliminary photograph(s)	rotation	
Type of diffractometer	CCD area detector	
Wavelength	0.71073 Å	
Data collection temperature	100(2) K	
Theta range for 9838 reflections used in lattice determination	4.655 to 65.411º	
Unit cell dimensions	a = 12.1351(9) Å	α= 90º
	b = 14.8021(10) Å	β= 98.642(3)º
	c = 22.944(2) Å	γ = 90º
Volume	4074.6(6) Å^3	
Z	4	
Crystal system	monoclinic	
Space group	P $2_1/c$	
Density (calculated)	1.356 g/cm^3	
F(000)	1744	

Theta range for data collection	2.2 to 33.2º
Completeness to theta = 25.242º	99.9%
Index ranges	$-17 \leq h \leq 18$, $-21 \leq k \leq 22$, $-34 \leq l \leq 34$
Reflections collected	125473
Independent reflections	14290 [R_{int}= 0.1065]
Reflections > 2s(I)	9560
Average s(I)/(net I)	0.1029
Absorption coefficient	0.59 mm^{-1}
Absorption correction	Semi-empirical from equivalents
Max. and min. transmission	0.7466 and 0.7034
Structure Solution and Refinement	
Hydrogen placement	geom
Refinement method	Full-matrix least-squares on F^2
Data / restraints / parameters	14290 / 0 / 460
Treatment of hydrogen atoms	constr
Goodness-of-fit on F^2	1.08
Final R indices [I>2s(I), 9560 reflections]	R1 = 0.0641, *w*R2 = 0.1225
R indices (all data)	R1 = 0.1239, *w*R2 = 0.1426
Type of weighting scheme used	calc
Max shift/error	0.001
Average shift/error	0.000
Extinction coefficient	n/a
Largest diff. peak and hole	2.73 and -0.90 e/$Å^{-3}$
Programs Used	
Structure refinement	SHELXL-2013 (Sheldrick, 2013)

^{1}H and ^{13}C NMR Spectra

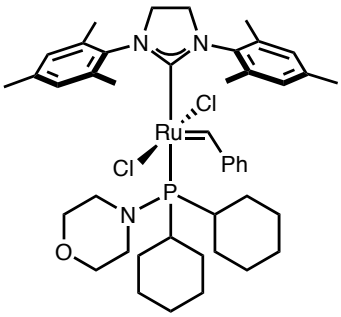
N
N
Cl
Ru
Cl
Ph
P
N
O

4-4

1.00
0.83
2.02
4.67
1.82
9.02
5.99
10.27
3.81
3.16
10.70
8.16
1.98
24
22
20
18
16
14
12
10
8
6
4
2
0

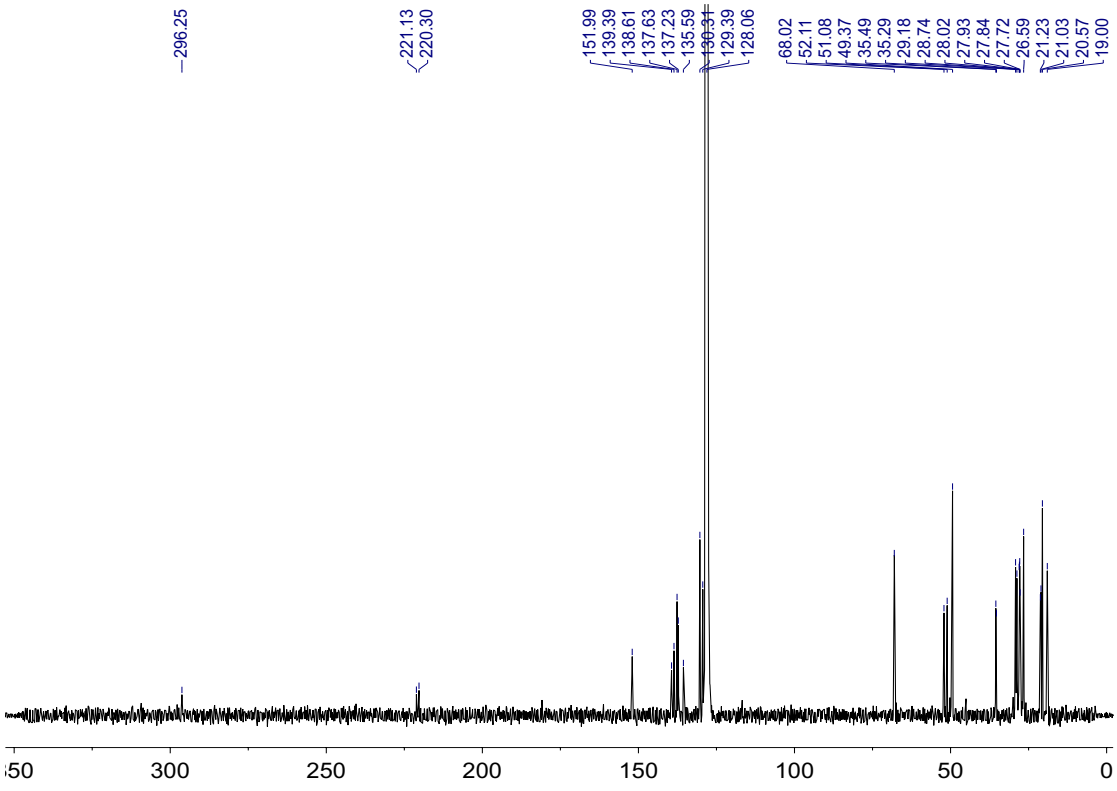
296.25
221.13
220.30
151.99
139.39
138.61
137.63
137.23
135.59
130.31
129.39
128.06
68.02
52.11
51.08
49.37
35.49
35.29
29.18
28.74
28.02
27.93
27.84
27.72
26.59
21.23
21.03
20.57
19.00
300
250
200
150
100
50
0

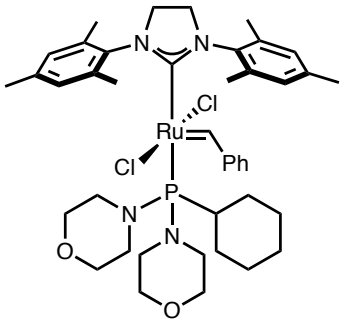
N
N
Cl
Ru
Cl
Ph
P
N
N
O
O

4-5

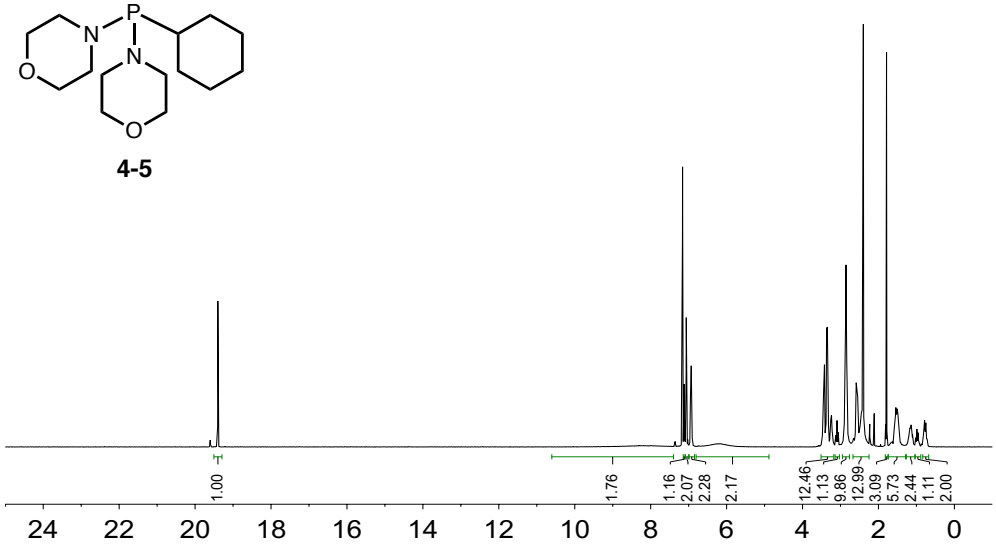
1.00
1.76
1.16
2.07
2.28
2.17
12.46
1.13
9.86
12.99
3.09
5.73
2.44
1.11
2.00
24
22
20
18
16
14
12
10
8
6
4
2
0

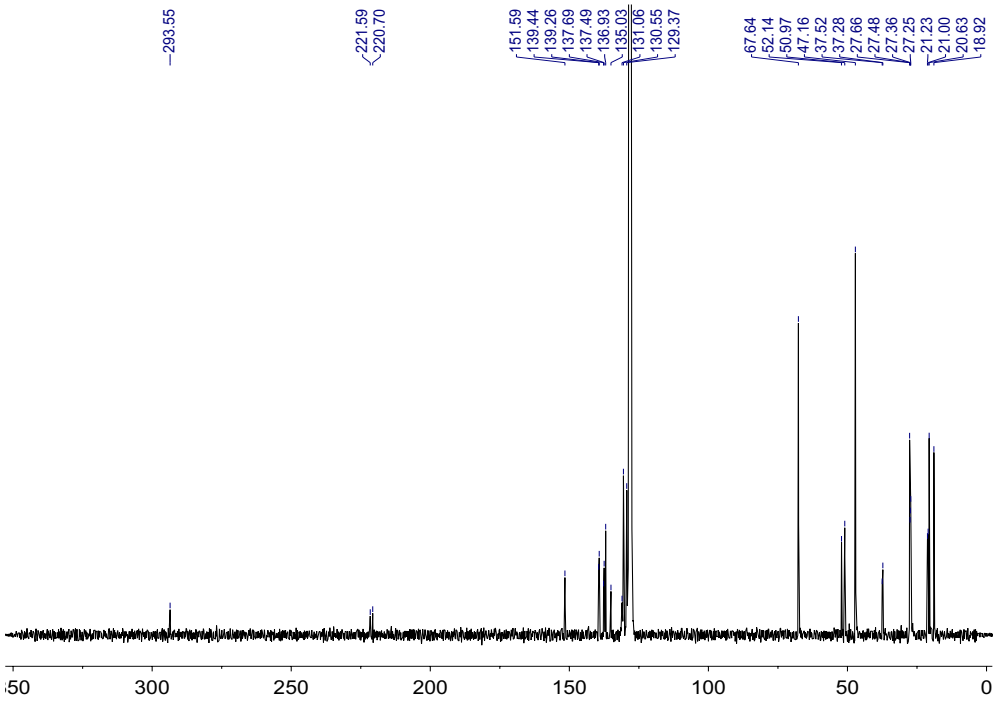
293.55
221.59
220.70
151.59
139.44
139.26
137.69
137.49
136.93
135.03
131.06
130.55
129.37
67.64
52.14
50.97
47.16
37.52
37.28
27.66
27.48
27.36
27.25
21.23
21.00
20.63
18.92
300
250
200
150
100
50
0

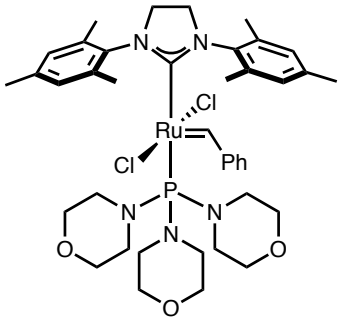
N
N
Cl
Ru
Cl
Ph
P
N
N
N
O
O
O

4-6

1.00
1.64
1.73
4.11
1.72
2.47
15.37
6.50
13.15
6.27
3.18
3.06
24
22
20
18
16
14
12
10
8
6
4
2
0

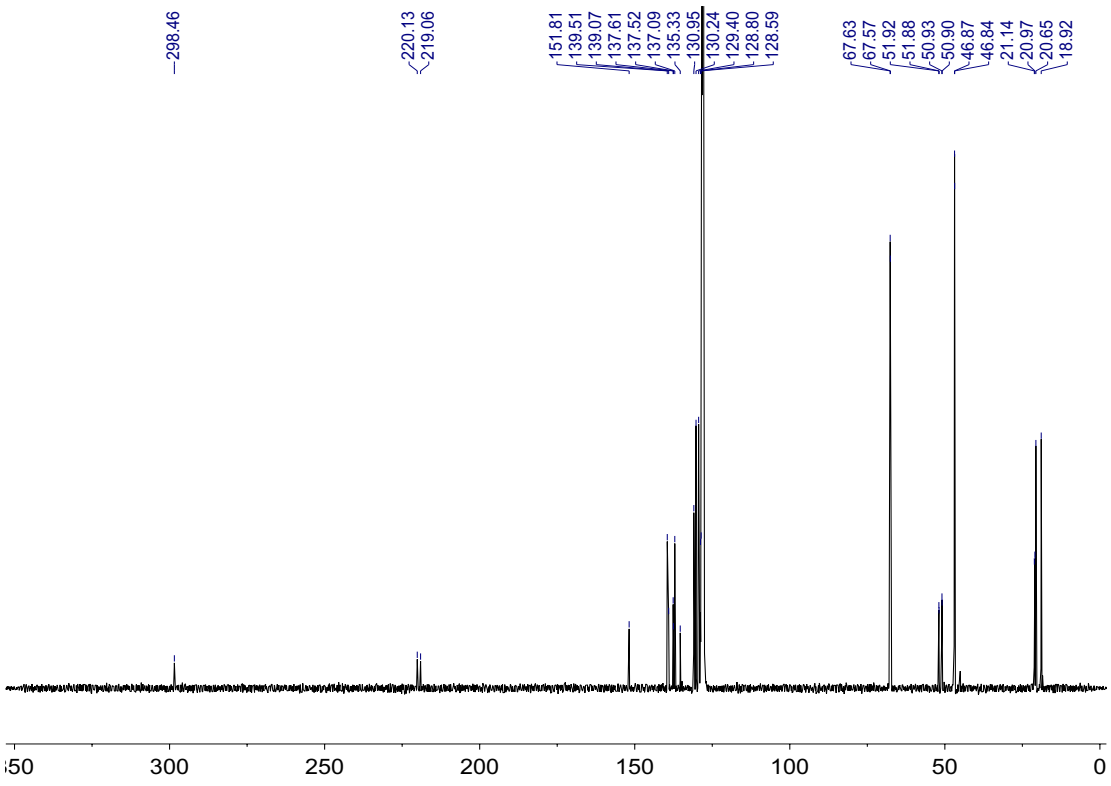
298.46
220.13
219.06
151.81
139.51
139.07
137.61
137.52
137.09
135.33
130.95
130.24
129.40
128.80
128.59
67.63
67.57
51.92
51.88
50.93
50.90
46.87
46.84
21.14
20.97
20.65
18.92
300
250
200
150
100
50
0

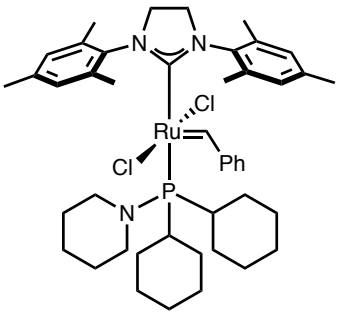
N
N
Cl
Ru
Cl
Ph
P
N

4-7

1.00
0.48
1.29
0.31
4.20
1.65
4.99
7.83
6.97
3.83
3.89
26.64
1.95
5 24 23 22 21 20 19 18 17 16 15 14 13 12 11 10 9 8 7 6 5 4 3 2 1
f1 (ppm)

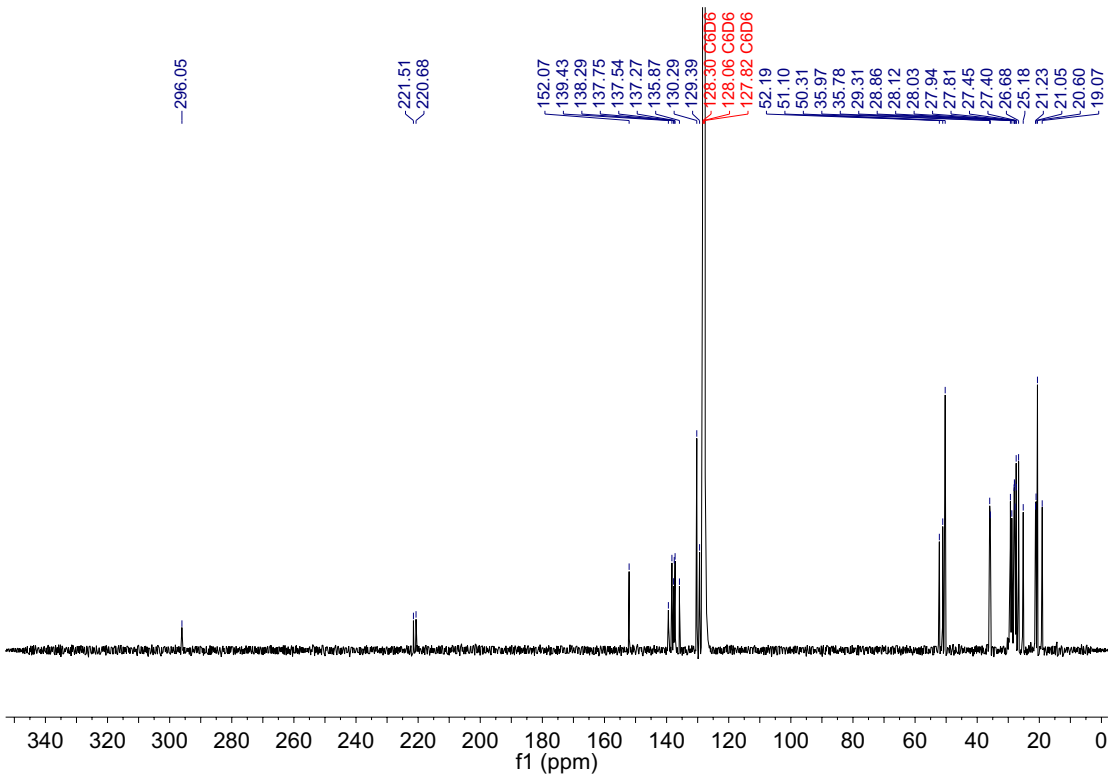
296.05
221.51
220.68
152.07
139.43
138.29
137.75
137.54
137.27
135.87
130.29
129.39
128.30 C6D6
128.06 C6D6
127.82 C6D6
52.19
51.10
50.31
35.97
35.78
29.31
28.86
28.12
28.03
27.94
27.81
27.45
27.40
26.68
25.18
21.23
21.05
20.60
19.07
340 320 300 280 260 240 220 200 180 160 140 120 100 80 60 40 20 0
f1 (ppm)

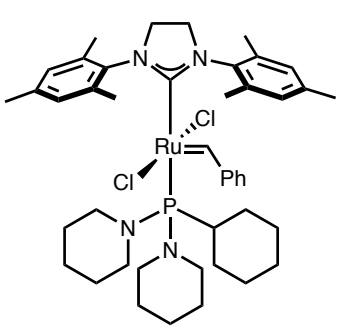
N
N
Cl
Ru
Cl
Ph
P
N
N

4-8

1.00
0.50
1.99
1.94
1.65
4.97
11.29
5.55
3.31
3.68
4.99
10.59
6.61
3.47
5 24 23 22 21 20 19 18 17 16 15 14 13 12 11 10 9 8 7 6 5 4 3 2 1 0
f1 (ppm)

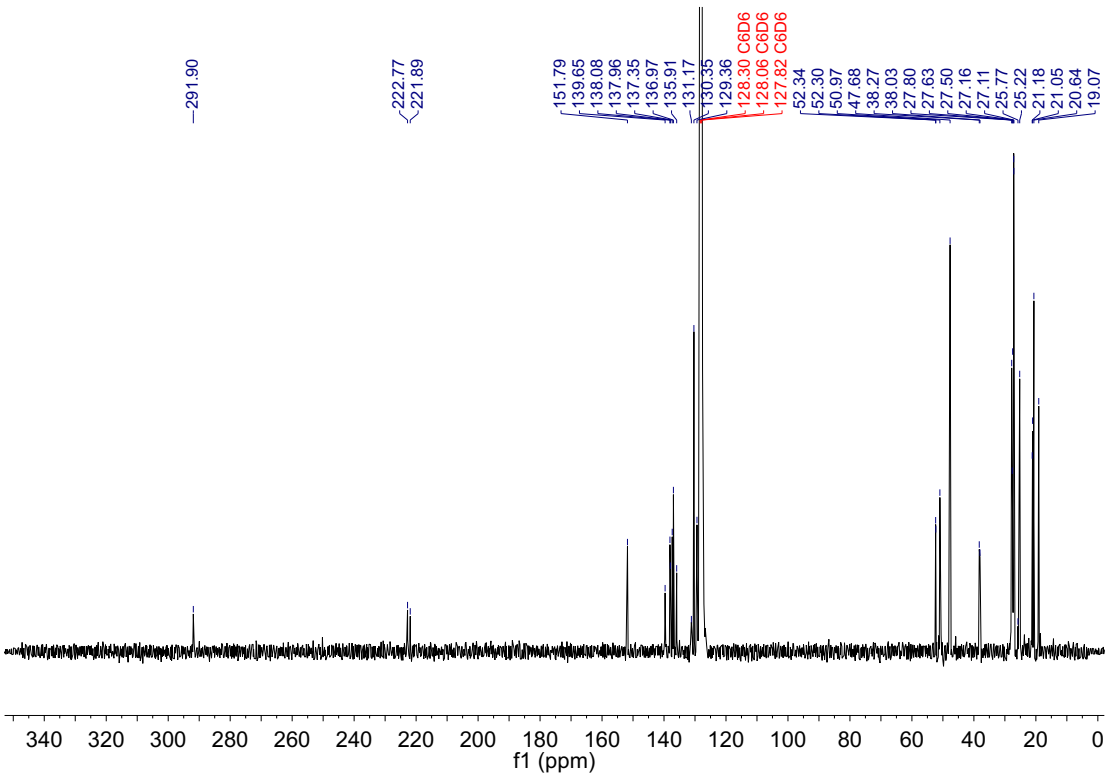
291.90
222.77
221.89
151.79
139.65
138.08
137.96
137.35
136.97
135.91
131.17
130.35
129.36
128.30 C6D6
128.06 C6D6
127.82 C6D6
52.34
52.30
50.97
47.68
38.27
38.03
27.80
27.63
27.50
27.16
27.11
25.77
25.22
21.18
21.05
20.64
19.07
340 320 300 280 260 240 220 200 180 160 140 120 100 80 60 40 20 0
f1 (ppm)

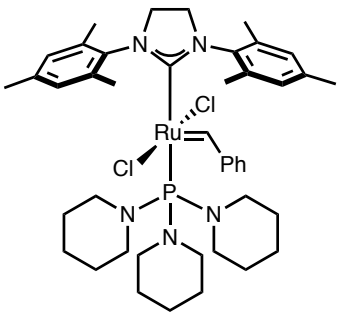
N
N
Cl
Ru
Cl
Ph
P
N
N
N

4-9

1.00
1.69
0.92
1.97
1.95
1.80
4.21
6.10
11.53
5.81
3.00
2.99
6.86
12.31
5 24 23 22 21 20 19 18 17 16 15 14 13 12 11 10 9 8 7 6 5 4 3 2 1 0
f1 (ppm)

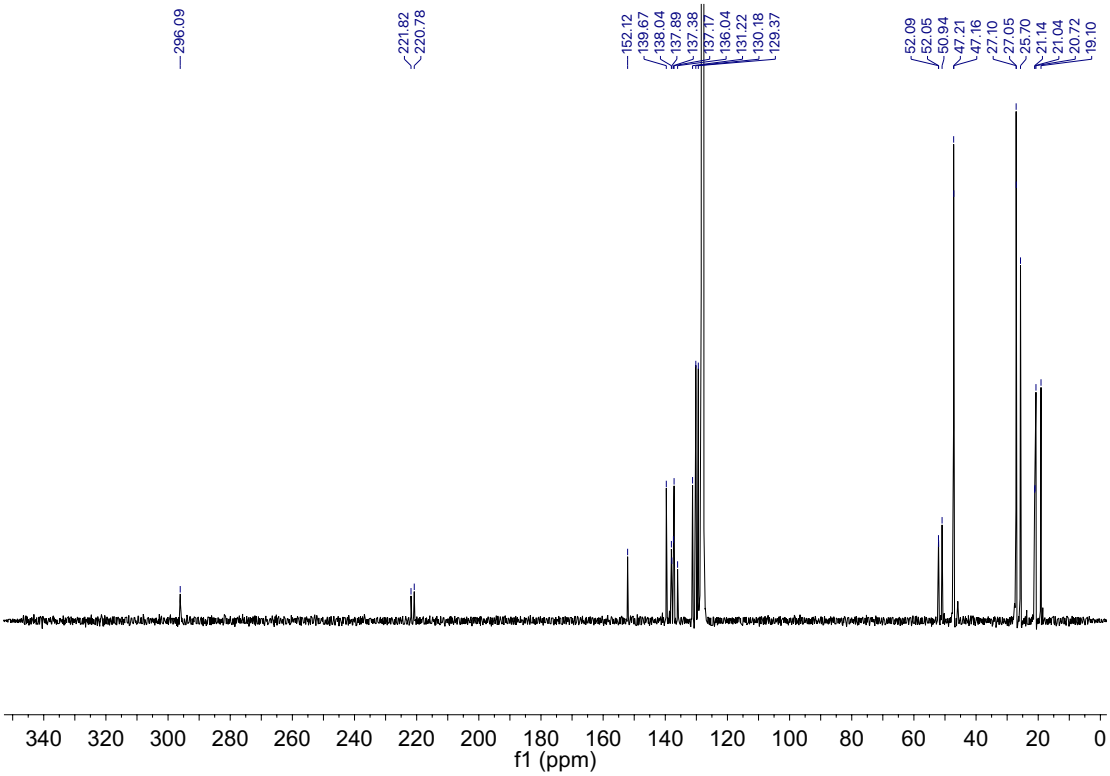
296.09
221.82
220.78
152.12
139.67
138.04
137.89
137.38
137.17
136.04
131.22
130.18
129.37
52.09
52.05
50.94
47.21
47.16
27.10
27.05
25.70
21.14
21.04
20.72
19.10
340 320 300 280 260 240 220 200 180 160 140 120 100 80 60 40 20 0
f1 (ppm)

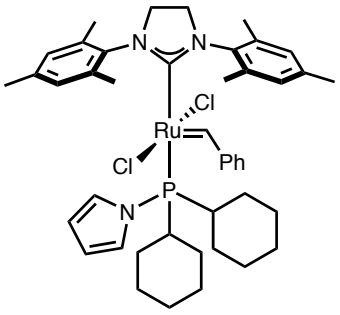
N
N
Cl
Ru
Cl
Ph
P
N

4-17

1.00
1.95
1.12
4.17
2.11
3.83
2.04
2.09
5.98
6.04
3.20
3.10
2.23
2.36
6.53
2.11
6.61
2.00
24
22
20
18
16
14
12
10
8
6
4
2
0

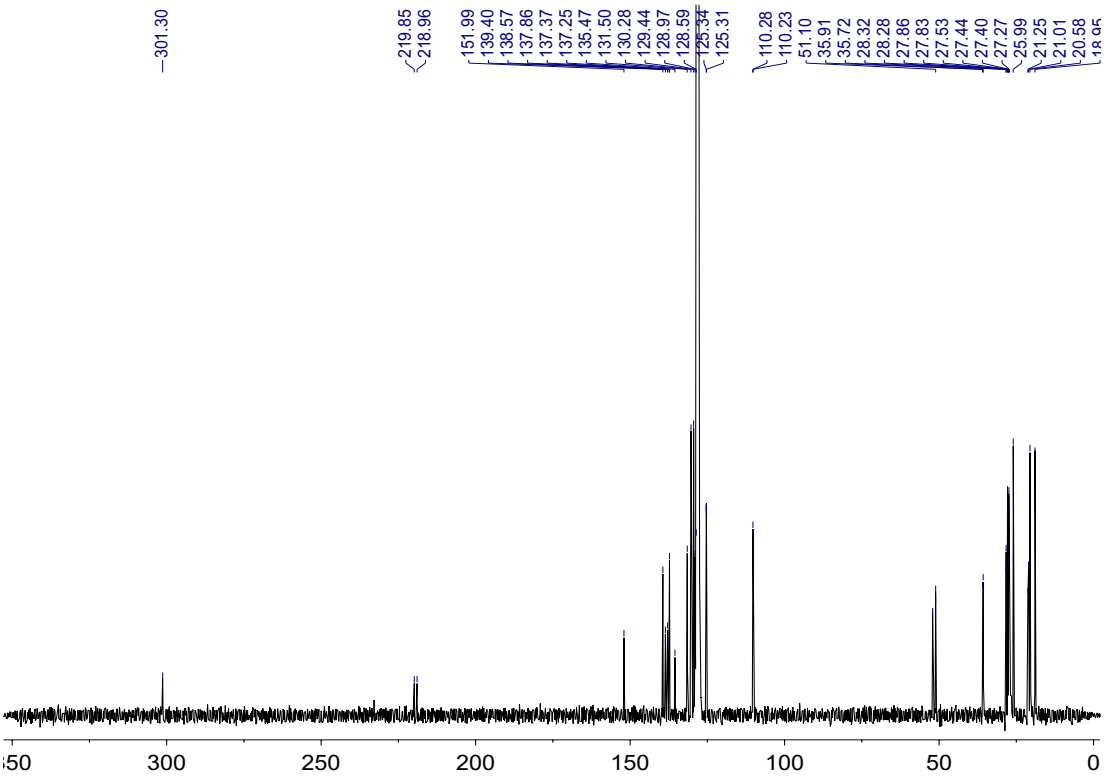
301.30
219.85
218.96
151.99
139.40
138.57
137.86
137.37
137.25
135.47
131.50
130.28
129.44
128.97
128.59
126.34
125.31
110.28
110.23
51.10
35.91
35.72
28.32
28.28
27.86
27.83
27.53
27.44
27.40
27.27
25.99
21.25
21.01
20.58
300
250
200
150
100
50
0

References

(1) For reviews, see: (a) Trnka, T. M.; Grubbs, R. H. *Acc. Chem. Res.* **2001,** *34*, 18-29. (b) Connon, S. J.; Blechert, S. *Angew. Chem., Int. Ed.* **2003,** *42*, 1900-1923. (c) Schrock, R. R.; Hoveyda, A. H. *Angew. Chem., Int. Ed.* **2003,** *42*, 4592-4633. (d) Grubbs, R. H. *Tetrahedron* **2004,** *60*, 7117-7140. (e) Hoveyda, A. H.; Zhugralin, A. R. *Nature* **2007,** *450*, 243-251. (f) Hoveyda, A. H. *J. Org. Chem.* **2014,** *79*, 4763-4792.

(2) For reviews on applications of metathesis in synthesis, see: (a) Fürstner, A. *Angew. Chem., Int. Ed.* **2000,** *39*, 3012-3043. (b) Monfette, S.; Fogg, D. E. *Chem. Rev.* **2009,** *109*, 3783-3816.

(3) For reviews on olefin metathesis polymerizations, see: (a) Buchmeiser, M. R. *Chem. Rev.* **2000,** *100*, 1565-1604. (b) Knall, A.-C.; Slugovc, C., Olefin Metathesis Polymerization. In *Olefin Metathesis*, John Wiley & Sons, Inc.: 2014; pp 269-284.

(4) For reviews related to ROMP, see: (a) Bielawski, C. W.; Grubbs, R. H. *Prog. Polym. Sci.* **2007,** *32*, 1-29. (b) Leitgeb, A.; Wappel, J.; Slugovc, C. *Polymer* **2010,** *51*, 2927-2946. (c) Schrock, R. R. *Acc. Chem. Res.* **2014,** *47*, 2457-2466.

(5) Atallah, P.; Wagener, K. B.; Schulz, M. D. *Macromolecules* **2013,** *46*, 4735-4741.

(6) Sutthasupa, S.; Shiotsuki, M.; Sanda, F. *Polym. J.* **2010,** *42*, 905-915.

(7) For examples of industrial applications of olefin metathesis, see: (a) Mol, J. C. *J. Mol. Catal. A: Chem.* **2004,** *213*, 39-45. (b) Slugovc, C., Industrial Applications of Olefin Metathesis Polymerization. In *Olefin Metathesis*, John Wiley & Sons, Inc.: 2014; pp 329-333.

(8) For early reports of olefin metathesis catalyzed by molybdenum and tungsten, see: (a) Schrock, R. R.; Feldman, J.; Cannizzo, L. F.; Grubbs, R. H. *Macromolecules* **1987,** *20*, 1169-1172. (b) Bazan, G. C.; Khosravi, E.; Schrock, R. R.; Feast, W. J.; Gibson, V. C.; O'Regan, M. B.; Thomas, J. K.; Davis, W. M. *J. Am. Chem. Soc.* **1990,** *112*, 8378.

(9) (a) Nguyen, S. T.; Johnson, L. K.; Grubbs, R. H.; Ziller, J. W. *J. Am. Chem. Soc.* **1992,** *114*, 3974-3975. (b) Nguyen, S. T.; Grubbs, R. H.; Ziller, J. W. *J. Am. Chem. Soc.* **1993,** *115*, 9858-9859.

(10) (a) Schwab, P.; France, M. B.; Ziller, J. W.; Grubbs, R. H. *Angew. Chem., Int. Ed. Engl.* **1995**, *34*, 2039-2041. (b) Schwab, P.; Grubbs, R. H.; Ziller, J. W. *J. Am. Chem. Soc.* **1996,** *118*, 100-110.

(11) Scholl, M.; Ding, S.; Lee, C. W.; Grubbs, R. H. *Org. Lett.* **1999,** *1*, 953-956.

(12) For reviews on ruthenium catalysts with NHC ligands, see: (a) Samojłowicz, C.; Bieniek, M.; Grela, K. *Chem. Rev.* **2009,** *109*, 3708-3742. (b) Vougioukalakis, G. C.; Grubbs, R. H. *Chem. Rev.* **2010,** *110*, 1746-1787.

(13) Getty, K.; Delgado-Jaime, M. U.; Kennepohl, P. *J. Am. Chem. Soc.* **2007,** *129*, 15774-15776.

(14) Love, J. A.; Morgan, J. P.; Trnka, T. M.; Grubbs, R. H. *Angew. Chem., Int. Ed.* **2002,** *41*, 4035-4037.

(15) Choi, T.-L.; Grubbs, R. H. *Angew. Chem., Int. Ed.* **2003,** *42*, 1743-1746.

(16) Sanford, M. S.; Love, J. A.; Grubbs, R. H. *Organometallics* **2001,** *20*, 5314-5318.

(17) (a) van der EideEdwin, F.; Piers, W. E. *Nat. Chem.* **2010,** *2*, 571-576. (b) Nelson, D. J.; Manzini, S.; Urbina-Blanco, C. A.; Nolan, S. P. *Chem. Commun.* **2014,** *50*, 10355-10375.

(18) Sanford, M. S.; Ulman, M.; Grubbs, R. H. *J. Am. Chem. Soc.* **2001,** *123*, 749-750.

(19) (a) Sanford, M. S.; Love, J. A.; Grubbs, R. H. *J. Am. Chem. Soc.* **2001,** *123*, 6543-6554. (b) Love, J. A.; Sanford, M. S.; Day, M. W.; Grubbs, R. H. *J. Am. Chem. Soc.* **2003,** *125*, 10103-10109.

(20) Moloy, K. G.; Petersen, J. L. *J. Am. Chem. Soc.* **1995,** *117*, 7696-7710.

(21) For studies related to the electronic properties of aminophosphines, see: (a) Kroshefsky, R. D.; Weiss, R.; Verkade, J. G. *Inorg. Chem.* **1979,** *18*, 469-472. (b) Barnard, T. S.; Mason, M. R. *Inorg. Chem.* **2001,** *40*, 5001-5009.

(22) Huang, J.; Stevens, E. D.; Nolan, S. P.; Petersen, J. L. *J. Am. Chem. Soc.* **1999,** *121*, 2674-2678.

(23) Maynard, H. D.; Okada, S. Y.; Grubbs, R. H. *Macromolecules* **2000,** *33*, 6239-6248.

(24) Equation 4.1 can be derived by applying the steady-state approximation to the 14-electron intermediate shown in Scheme 4.1. See ref. 19a.

(25) Lin, T.-P.; Chang, A. B.; Chen, H.-Y.; Liberman-Martin, A. L.; Bates, C. M.; Voegtle, M. J.; Bauer, C. A.; Grubbs, R. H. *J. Am. Chem. Soc.* **2017,** *139*, 3896-3903.

(26) Computational studies were performed by graduate student Huiling Shao and Professor Peng Liu of the University of Pittsburgh.